X-ray spectra and polarization from magnetar candidates

R. Taverna,[1,2]⋆ R. Turolla,[2,3]⋆ V. Suleimanov,[4,5,6] A. Y. Potekhin[7] and S. Zane[3]⋆

[1]*Department of Mathematics and Physics, University of Roma Tre, via della Vasca Navale 84, I-00146 Roma, Italy*

[2]*Department of Physics and Astronomy, University of Padova, via Marzolo 8, I-35131 Padova, Italy*

[3]*Mullard Space Science Laboratory, University College London, Holmbury St. Mary, Surrey RH5 6NT, UK*

[4]*Institut für Astronomie und Astrophysik, Sand 1, D-72076 Tübingen, Germany*

[5]*Kazan (Volga region) Federal University, Kremlevskaja str, 18, Kazan 420008, Russia*

[6]*Space Research Institute of the Russian Academy of Sciences, Profsoyuznaya Str 84/32, Moscow 117997, Russia*

[7]*Ioffe Institute, Politekhnicheskaya 26, Saint Petersburg 194021, Russia*

ABSTRACT

Magnetars are believed to host the strongest magnetic fields in the present universe ($B \gtrsim 10^{14}$ G) and the study of their persistent emission in the X-ray band offers an unprecedented opportunity to gain insight into physical processes in the presence of ultra-strong magnetic fields. Up to now, most of our knowledge about magnetar sources came from spectral analysis, which allowed to test the resonant Compton scattering scenario and to probe the structure of the star magnetosphere. On the other hand, radiation emitted from magnetar surface is expected to be strongly polarized and its observed polarization pattern bears the imprint of both scatterings on to magnetospheric charges and quantum electro-dynamics (QED) effects as it propagates in the magnetized vacuum around the star. X-ray polarimeters scheduled to fly in the next years will finally allow to exploit the wealth of information stored in the polarization observables. Here we revisit the problem of assessing the spectro-polarimetric properties of magnetar persistent emission. At variance with previous investigations, proper account for more physical surface emission models is made by considering either a condensed surface or a magnetized atmosphere. Results are used to simulate polarimetric observations with the forthcoming Imaging X-ray Polarimetry Explorer. We find that X-ray polarimetry will allow to detect QED vacuum effects for all the emission models we considered and to discriminate among them.

Key words: polarization – radiative transfer – scattering – techniques: polarimetric – stars: magnetars – X-rays: stars.

1 INTRODUCTION

Anomalous X-ray pulsars (AXPs) and soft-gamma repeaters (SGRs) stand up as peculiar objects amongst the varied landscape of neutron star (NS) sources. The measured spin periods ($P \approx 2$–12 s) and spin-down rates ($\dot{P} \approx 10^{-15}$ to 10^{-10} s s^{-1}) set them apart from the bulk of the NS population, and point to ultra-strong dipole magnetic fields (up to 10^{14}–10^{15} G), orders of magnitude higher than those of ordinary NSs. Nowadays, a wide consensus gathered in favour of the presence of an ultra-magnetized NS, a magnetar, in AXPs/SGRs, following the original suggestion by Duncan & Thompson (1992) and Thompson & Duncan (1995, see Turolla, Zane & Watts 2015; Kaspi & Beloborodov 2017 for recent reviews). Observationally, AXPs and SGRs manifest themselves through the emission of short X-ray bursts (with luminosities $L_X \approx 10^{36}$–10^{43} ergs^{-1} and duration $\Delta t \approx 0.01$–50 s) and, exceptionally, of much more energetic giant flares ($L_X \approx 10^{44}$–10^{47} ergs^{-1} and $\Delta t \approx 100$–1000 s). Presently, the list of magnetar sources totals more than 20 objects (plus some candidates; Olausen & Kaspi 2014[1]), many of which are transients, detectable only during their outburst phases, when the flux increases up to a factor $\approx 10^3$ above the quiescent level (see e.g. Rea & Esposito 2011).

Magnetars exhibit also a persistent emission in the ≈ 0.5–200 keV band, with $L_X \approx 10^{31}$–10^{36} ergs^{-1}, usually in excess of the rotational energy loss rate, $\dot{E}_{rot} \sim 4 \times 10^{46} \dot{P}/P^3$ erg s^{-1}. In the soft X-rays (0.1–10 keV), the spectrum is typically the superposition of a thermal component ($kT \approx 1$ keV) and a power-law tail (photon index $\Gamma \approx 2$–4), although transient sources often show a purely thermal

[1]See the McGill magnetar catalogue: http://www.physics.mcgill.ca/ pulsar /magnetar/main.html

spectrum. Up to now, many of the magnetar emission properties have been unveiled by investigating their spectra; this also allowed to shed light on how thermal photons are reprocessed in the star magnetosphere, supporting the resonant Compton scattering (RCS) paradigm (see Thompson et al. 2002).

The extremely strong magnetic field near the surface of a magnetar implies that radiation is highly polarized. This is due to the effects of the magnetic field on the optical properties of both the plasma and the vacuum in which the photons propagate (see e.g. Harding & Lai 2006, for a review). Polarimetric observations in the X-rays are bound to add a new dimension to our knowledge of magnetars, by providing, among others, an independent estimate of the magnetic field strength and topology and by unveiling the source geometry (Fernández & Davis 2011; Taverna et al. 2014; Taverna & Turolla 2017). At variance with spectral measurements, the wealth of information encoded in polarization observables is still to be exploited. In fact, previous efforts with the *OSO-8* satellite (Weisskopf et al. 1978) and balloon experiments (e.g. *PoGO/PoGOLite*; Larsson & Pearce 2004; Kiss & Pearce 2007) were limited only to a couple of very bright sources with large enough polarization degree. Full-fledged polarimetric missions finally started to be planned in the last decade and culminated in the Imaging X-ray Polarimetry Explorer *(IXPE)* observatory (Weisskopf et al. 2016), a NASA-ASI SMEX mission scheduled to fly in 2021, and in the *eXTP* satellite (Zhang et al. 2019), approved by the Chinese Academy of Science.

Goal of this paper is to provide a systematic assessment of the spectral and polarization properties of magnetar persistent emission in the 2–10 keV band, the working energy range of new-generation polarimeters. In particular, we take a step beyond previous treatments of RCS in magnetar magnetospheres by considering different surface emission models which are more physically motivated, a magnetized atmosphere and a condensed surface, in place of simple blackbody emission. Spectro-polarimetric calculations are finalized to produce synthetic data for *IXPE* in order to evaluate the detectability of magnetar sources and the capability of the instrument in disentangling different physical situations.

The plan of the paper is as follows. The theoretical framework is set up in Section 2, while Section 3 contains a description of the numerical techniques used to compute spectra and polarization observables. Results are presented in Section 4 and simulations of *IXPE* observations are reported in Section 5. Discussion and conclusions follow in Section 6.

2 THE MODEL

The spectral properties of the persistent emission from magnetar sources have been successfully modelled in terms of the RCS paradigm, as originally suggested by Thompson et al. (2002). According to this scenario, thermal photons emitted by the cooling star surface are resonantly up-scattered by charges flowing along the closed field lines of a non-potential (twisted) magnetic field. This is expected to produce a thermal spectrum with an extended power-law like tail in the 0.1–10 keV energy range. Detailed calculations, based on Monte carlo simulations, confirmed this picture (Fernández & Thompson 2007; Nobili, Turolla & Zane 2008), and their application to spectral fitting of SGRs/AXPs allowed to estimate the physical parameters of magnetar magnetospheres (Zane et al. 2009). Following the same approach, the expected polarization pattern in magnetars has been also investigated in the wake of the growing interest in X-ray polarimetry (Fernández & Davis 2011; Taverna et al. 2014; Güver, Göğüş & Özel 2015).

Photons propagating in a strongly magnetized vacuum are expected to be elliptically polarized in two normal modes, the ordinary (O) and the extraordinary (X) ones, with the photon electric field mainly oscillating either parallel or perpendicular to the plane of the photon propagation direction and the local magnetic field, respectively (Gnedin & Pavlov 1973, see also Harding & Lai 2006). Here we assume that radiation is linearly polarized in the two modes. The observed polarization pattern depends on the intrinsic polarization of the surface thermal radiation, on scatterings in the magnetosphere and on QED effects (vacuum birefringence, see Heyl & Shaviv 2000, 2002; Fernández & Davis 2011; Taverna et al. 2014, 2015; González Caniulef et al. 2016). Previous investigations of photon reprocessing in the magnetar magnetosphere adopted the simplifying assumption of 100 per cent polarized (either in the X or O mode) blackbody radiation for surface emission.[2] Hence, more realistic models for surface emission should be considered to better characterize the spectral and polarization properties of magnetar persistent emission within the RCS scenario, as discussed below.

2.1 Thermal emission from NS surface

The properties of the outermost layers of a highly magnetized NS are still debated. According to the commonly accepted picture, NSs should be covered by a gaseous atmosphere, with typical scale height $H \sim kT/m_\mathrm{p}g \approx 0.1$–10 cm, with T the surface temperature, m_p the proton mass, and g the surface gravity. Model atmospheres have been investigated by many authors, allowing for different chemical compositions (H, He, and heavy elements) and magnetization (see e.g. Romani 1987; Shibanov et al. 1992; Pavlov et al. 1994; Potekhin 2014, for a recent review). On the other hand, magnetic fields strong enough that the electron gyroradius becomes smaller than the Bohr radius ($B \gtrsim 2.4 \times 10^9$ G) change substantially the properties of matter. Under such conditions, highly elongated atoms can form molecular chains and this can result in a phase transition which turns the star surface into a condensate (either liquid or solid, see Lai & Salpeter 1997). The critical temperature T_crit for condensation depends on the magnetic field and on the composition (Lai 2001; Medin & Lai 2007). In magnetar sources, where $B \gtrsim 10^{14}$ G, magnetic condensation is expected to take place also at temperatures in excess of 0.1 keV for heavy element compositions, in the same range of those inferred from X-ray observations. Indeed, as it can be seen from Fig. 1, some magnetars lie within the condensation region, while others, the 'low-field' SGR 0418+5729 in particular (see Rea et al. 2010), do not. We note, however, that the values of B and T used to mark the position of magnetar sources in the plot are taken from the McGill catalogue (Olausen & Kaspi 2014). This means that T is the blackbody temperature (as obtained from the spectral fit) and B is the dipole field (as derived from the spin-down measure at the magnetic equator). Actually, estimates of the emitting area indicate that thermal photons come from a heated cap, while the rest of the surface is cooler (typically ≈ 1 versus ≈ 0.1 keV; see e.g. the discussion in Albano et al. 2010, for the AXPs XTE J1810–197 and CXOU J164710.2–455216). In this respect, the temperatures reported in Fig. 1 are likely an overestimate, since the (single) blackbody fit samples the hottest component most. It is also possible that surface condensation depends on the (magnetic) co-latitude, with the cooler equatorial belt undergoing a phase transition

---

[2]The predominance of extraordinary photons can be justified on the basis of the reduced opacity for the X-mode (see e.g. Pavlov & Shibanov 1978; Mészáros 1992, see also Lai & Ho 2002).
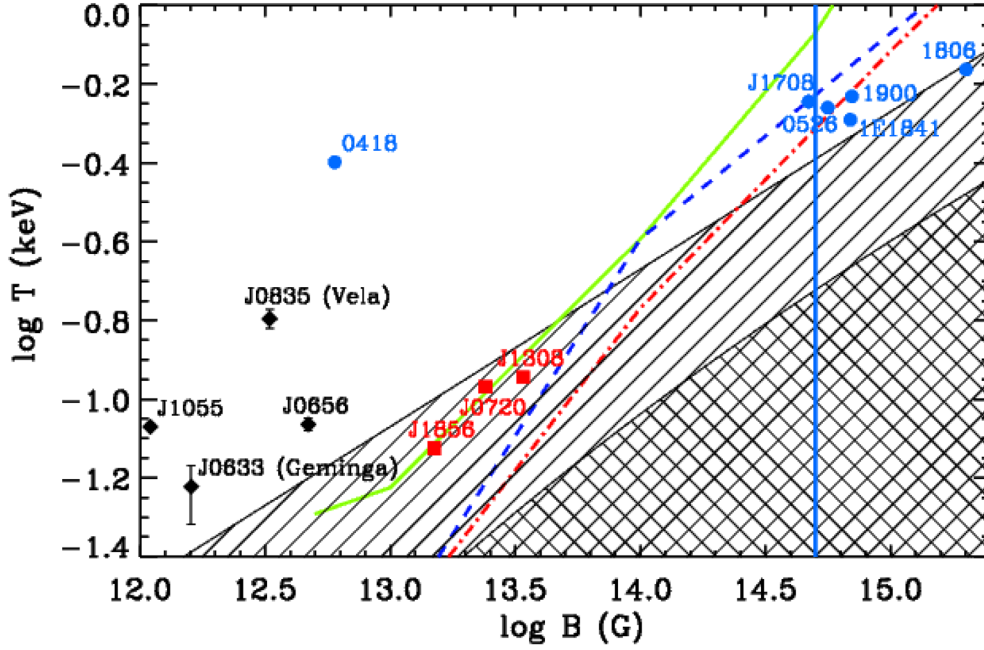
Figure 1. The critical temperature for magnetic condensation as a function of the surface field. The lines refer to different chemical compositions: iron (green, solid), carbon (blue, dashed), and helium (red, dash–dotted), according to the calculations by Medin & Lai (2006, 2007). The shaded and hatched areas mark the condensation regions for Fe and H, respectively, according to the older estimate by Lai (2001). Samples of different NS sources are marked with different symbols: cyan filled circles (magnetars; see Olausen & Kaspi 2014[1]), red squares and black diamonds (X-ray dim isolated NSs and isolated pulsars, respectively; see Turolla 2009). The thick vertical line is drawn in correspondence to a magnetic field of 5×10^{14} G.

and the hotter caps not. The local, surface strength of the *B*-field, which is not likely to coincide with the spin-down value, is also key in producing the condensation.

Similar considerations have been already presented in analysing the polarization properties of thermal emission from X-ray Dim Isolated Neutron Stars and magnetars by González Caniulef et al. (2016, 2017, see also Santangelo et al. 2019a), who also explored a gaseous atmosphere and a condensed surface. Magnetar RCS spectral and polarimetric models were investigated in the idealized case of BB seed photons (Fernández & Thompson 2007; Nobili, Turolla & Zane 2008; Zane et al. 2009; Fernández & Davis 2011; Taverna et al. 2014). An exception is the work by Güver et al. (2015), in which modelling of the spectral properties of the AXP 1E 1048.1–5937 was carried out assuming that thermal surface radiation comes from a magnetized, fully ionized H atmosphere. In this investigation we consider surface emission from both a magnetized H atmosphere and a condensed surface. The main features of the models we use are discussed below. In the following all calculations refer to an NS with mass $M_{NS} = 1.5 \, M_\odot$ and radius $R_{NS} = 12$ km (which correspond to a surface gravity $g_{NS} = 1.4 \times 10^{14}$ cm s^{-2}).

### 2.1.1 Magnetized atmosphere

Highly magnetized plane-parallel NS atmospheres are computed using the code described in Suleimanov, Potekhin & Werner (2009), suitably modified to account for different inclinations θ_B of the magnetic field with respect to the local surface normal. Only a pure-hydrogen composition is considered and partial ionization in strong magnetic fields is properly treated (see e.g. Potekhin et al. 2004). Vacuum polarization effects (the Mikheyev–Smirnov–Wolfenstein resonance) are included and mode switching is treated following van Adelsberg & Lai (2006). The opacities, polarizabilities, and

Table 1. Values of the magnetic colatitude Θ_s, magnetic field strength B, and inclination θ_B used for the magnetized atmosphere models (here $B_p = 5 \times 10^{14}$ G).

N	$\cos \Theta_s$	$B/10^{14}$ G	$\cos \theta_B$
1	0.05	2.40809	0.101399
2	0.15	2.47787	0.295411
3	0.25	2.61143	0.466226
4	0.35	2.79889	0.607170
5	0.45	3.02928	0.718498
6	0.55	3.29254	0.804283
7	0.65	3.58034	0.869697
8	0.75	3.88628	0.919553
9	0.85	4.20559	0.957813
10	0.95	4.53447	0.987560

equation of state of the hydrogen plasma were computed, using the updated approach discussed in Potekhin, Chabrier & Ho (2014), on a fixed grid of plasma temperature and density, from which the values required during the actual calculation were obtained by interpolation. For the sake of comparison with previous works (Nobili et al. 2008; Taverna et al. 2014) and also because of the lack of a more accurate model, the surface temperature is assumed to be constant (a more thorough discussion on the limitations and the effects of this assumption on our results is presented in Section 6). The output (i.e. the specific intensities I_X and I_O for X- and O-mode photons, respectively) was produced for a selected sample of magnetic field strengths and inclinations (see Table 1).

Model atmospheres for an inclined magnetic field require much longer computational times with respect to the aligned case, essentially because the transfer problem must be now solved in two dimensions instead of one, due to the loss of symmetry around the surface normal (i.e. the specific intensity depends now on both
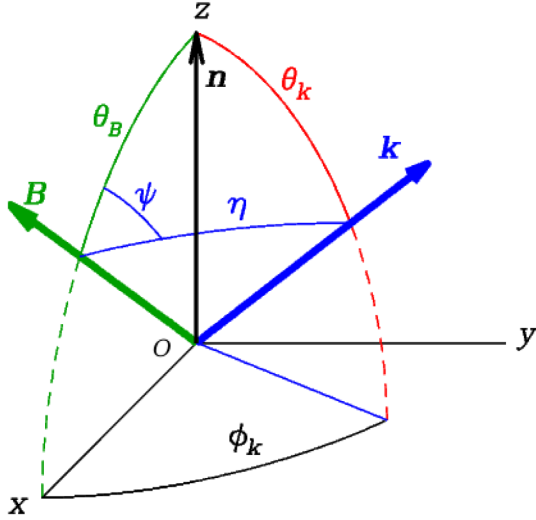
Figure 2. Emission geometry for a small element on the NS surface centred in O. The z-axis is along the surface normal $\boldsymbol{n}$, while $\boldsymbol{B}$ and $\boldsymbol{k}$ are the local magnetic field and the unit vector along the line-of-sight, respectively. The direction of $\boldsymbol{k}$ in the xyz frame is fixed by the pair of polar angles θ_{k} and ϕ_{k}. The angles η and ψ provide again the direction of $\boldsymbol{k}$, but this time with respect to $\boldsymbol{B}$. Finally, θ_B gives the inclination of $\boldsymbol{B}$ with respect to the surface normal.

the polar angles and not on the co-latitude alone; see below). The optical properties of the magnetized plasma depend on the angle η between the photon propagation direction $\boldsymbol{k}$ and the local magnetic field $\boldsymbol{B}$. On the other hand, under the plane-parallel approximation the radiation field naturally depends on the angle θ_{k} between $\boldsymbol{k}$ and the surface normal $\boldsymbol{n}$ (see Fig. 2). In the aligned case ($\theta_B = 0$), η and θ_{k} coincide; this allows to solve the radiative transfer equation over a one-dimensional θ_{k} angular grid, exploiting the axial symmetry of the specific intensity around $\boldsymbol{B} \equiv \boldsymbol{n}$. On the other hand, for $\theta_B \neq 0$ the symmetry is lost and the transfer equation should be solved on a two-dimensional (θ_{k}, ϕ_{k}) grid, with ϕ_{k} the azimuth associated with θ_{k}. To avoid the interpolation of the opacities over such a two-dimensional grid, the code solves the transfer problem over an (η, ψ) angular grid, with ψ the azimuth associated with η (see Fig. 2). However, in order to compute integrals over the NS surface one needs anyway to know the values of θ_{k} and ϕ_{k} corresponding to each point in the (η, ψ) grid. These can be obtained through a spherical polar coordinate transformation

$$\cos\theta_{\mathrm{k}} = \cos\theta_B \cos\eta + \sin\theta_B \sin\eta \cos\psi$$

$$\cos\phi_{\mathrm{k}} = \frac{\sin\theta_B \cos\eta - \cos\theta_B \sin\eta \cos\psi}{\sin\theta_{\mathrm{k}}}$$

$$\sin\phi_{\mathrm{k}} = \frac{\sin\eta \sin\psi}{\sin\theta_{\mathrm{k}}}, \tag{1}$$

where the correct value of ϕ_{k} depends on the signs of both $\cos\phi_{\mathrm{k}}$ and $\sin\phi_{\mathrm{k}}$. Actually, only the models corresponding to the northern magnetic hemisphere ($\cos\theta_B > 0$) need to be computed. In the Southern hemisphere the replacement $\phi_{\mathrm{k}} \to \pi - \phi_{\mathrm{k}}$ holds for the patches characterized by $\theta_B > \pi$ because of the symmetry properties of the opacities (see e.g. González Caniulef et al. 2016).[3] This

[3] As it will be discussed later on, actual calculations refer to a globally twisted dipole field, which however possesses the same north–south symmetry as a dipolar field (see Thompson et al. 2002; Pavan et al. 2009).

relation translates into $\eta \to \pi - \eta$ in the coordinate system referred to $\boldsymbol{B}$, as it can be checked using equations (1). The specific intensity emerging from the atmosphere is shown in Fig. 3 for three models with different magnetic field strength and inclination, and $T_{\mathrm{eff}} = 0.5\,\mathrm{keV}$ (# 1, 7, and 10 in table 1); results refer to $\phi_{\mathrm{k}} = 0$ and different values of θ_{k}. A distinctive feature is the presence of a narrow proton cyclotron line in absorption at $E_{\mathrm{Bp}} \sim 0.63(B/10^{14}\,\mathrm{G})$; the high degree of anisotropy in the emission is clearly seen by comparing the different curves in each panel.

In a twisted magnetosphere charges flow along the close magnetic field lines. This implies that returning currents hit the star surface, heating the star external layers (see Beloborodov & Thompson 2007; Fernández & Davis 2011). Investigations on the effects of backflowing charges on the atmospheres have started (González Caniulef et al. 2019), but a complete study is still lacking. For this reason, in this work we consider a passively cooling, magnetized atmosphere, neglecting all the possible effects of returning currents (see again Section 6 for a more comprehensive discussion).

2.1.2 Condensed surface

Thermal radiation coming from a bare NS was first studied by Brinkmann (1980) and further investigated by (Turolla, Zane & Drake 2004; Pérez-Azorín, Miralles & Pons 2005; van Adelsberg et al. 2005; Potekhin et al. 2012, see also Potekhin 2014 for a recent review). In these papers, the calculation of the intensity and polarization of radiation emitted by a condensed surface was based on the (complex) dielectric tensor in the medium just below the condensed surface, derived in the cold plasma approximation (see e.g. Ginzburg 1970). It should be noted that this formalism allows to treat not only reflection and transmission of an electromagnetic wave, but also true absorption, which enters the equations through the imaginary part of the indices of refraction. The monochromatic intensities of the two independent polarization modes $\ell = 1$, 2 emitted by a heated condensed surface[4] can be written as (see van Adelsberg et al. 2005)

$$I_{v,\ell} = j_{v,\ell} B_v/2 = (1 - R_{v,\ell}) B_v/2, \tag{2}$$

where B_v is the Planck spectral radiance, $j_{v,\ell}$ are the (normalized) emissivities, and $R_{v,\ell}$ the reflectivities. The latter can be derived by considering the reflected and transmitted electromagnetic fields ($\boldsymbol{E}_\ell^{(\mathrm{r})}$ and $\boldsymbol{E}_\ell^{(\mathrm{t})}$) that arise in response to the incidence of an arbitrary linearly polarized wave on the surface, with electric field $\boldsymbol{E}_\ell^{(\mathrm{i})} = \mathcal{A}_\ell \boldsymbol{e}_\ell^{(\mathrm{i})}$,

$$\boldsymbol{E}_\ell^{(\mathrm{r})} = \mathcal{A}_\ell \sum_{m=1}^{2} r_{m\ell} \boldsymbol{e}_m^{(\mathrm{r})}, \qquad \boldsymbol{E}_\ell^{(\mathrm{t})} = \mathcal{A}_\ell \sum_{m=1}^{2} t_{m\ell} \boldsymbol{e}_m^{(\mathrm{t})}; \tag{3}$$

here $\mathcal{A}_\ell$ are the complex amplitudes of the electric field of the incoming wave, $\boldsymbol{e}_\ell^{(\mathrm{i})}$, $\boldsymbol{e}_\ell^{(\mathrm{r})}$, and $\boldsymbol{e}_\ell^{(\mathrm{t})}$ are the unit polarization vectors and $r_{m\ell}$ and $t_{m\ell}$ are complex coefficients. The dimensionless reflectivities for the two orthogonal linear polarizations can be expressed as
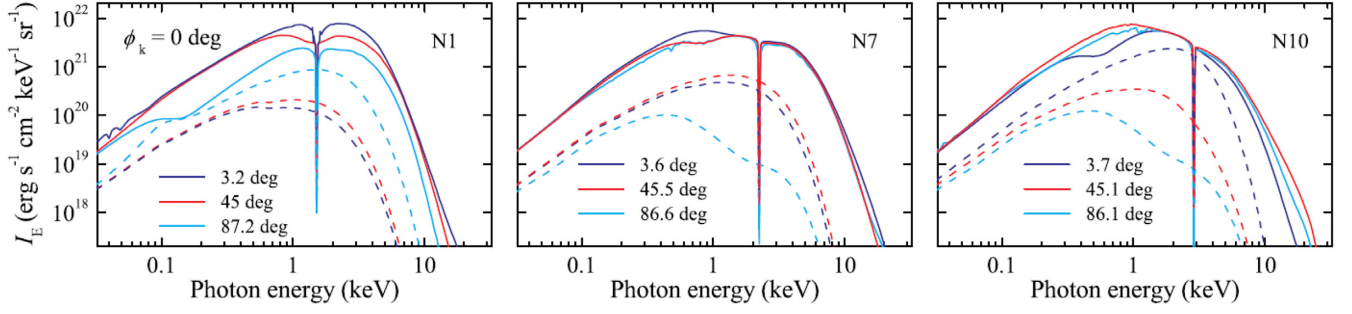
$$R_{v,\ell} = |r_{\ell 1}|^2 + |r_{\ell 2}|^2. \tag{4}$$

The coefficients $r_{m\ell}$ are in turn obtained from Maxwell's equations for the transmitted modes

$$\left[\boldsymbol{\epsilon} + n_\ell^2 \left(\boldsymbol{k}_\ell^{(\mathrm{t})} \otimes \boldsymbol{k}_\ell^{(\mathrm{t})} - \mathbb{1} \right) \right] \cdot \boldsymbol{E}_\ell^{(\mathrm{t})} = \boldsymbol{0}, \tag{5}$$

[4] Modes 1 and 2 are defined as perpendicular and parallel, respectively, to the plane of the photon direction $\boldsymbol{k}$ and the local surface normal $\boldsymbol{n}$.

Figure 3. Spectral distributions of the specific intensities I_X (solid lines) and I_O (dashed lines) for different values of θ_k (marked on each panel) and $\phi_k = 0°$, for the models 1 (left), 7 (centre), and 10 (right, see Table 1). Here the effective temperature is $T_{eff} = 0.5$ keV.

where $\boldsymbol{\epsilon}$ is the dielectric tensor of the medium, n_ℓ is the index of refraction for mode ℓ, $\boldsymbol{k}_\ell^{(t)}$ is the (transmitted) unit wavevector, and $\mathbb{1}$ is the unit tensor. Maxwell's boundary conditions connect $r_{m\ell}$ with $t_{m\ell}$, thus closing this set of equations.

The exact form of $\boldsymbol{\epsilon}$ is currently unknown. One usually applies the approximation of a fully ionized electron-ion plasma with either non-moving ions (the so-called fixed-ion limit) or finite-mass ions freely responsive to the electromagnetic forces (free-ion limit). In reality, however, there are Coulomb forces between the ions, which hamper the ion response, but still cannot completely 'freeze' the ions in their equilibrium positions. The problem is further complicated by the possibility of incomplete ionization, i.e. the existence of bound electron shells embedded in the plasma, which may be anticipated in a shallow layer beneath the surface.

In the following we use the analytical, approximating formulae developed by Potekhin et al. (2012, see also González Caniulef et al. 2016), which provide the emissivities $j_{\nu,\ell}$ as functions of the magnetic field strength B, the photon energy $h\nu$, the angle θ_B and the polar angles θ_k and ϕ_k between the local normal $\boldsymbol{n}$ to the star surface and the photon direction $\boldsymbol{k}$. The expressions for the emissivities $j_{\nu,X}$ and $j_{\nu,O}$ in the X and O modes are then obtained from $j_{\nu,1}$ and $j_{\nu,2}$ through a rotation in the plane orthogonal to $\boldsymbol{k}$, which amounts to write

$$j_{\nu,O} = \left(\boldsymbol{x}'_r \cdot \boldsymbol{e}_1^{(r)}\right)^2 j_{\nu,1} + \left(\boldsymbol{x}'_r \cdot \boldsymbol{e}_2^{(r)}\right)^2 j_{\nu,2}$$

$$j_{\nu,X} = \left(\boldsymbol{y}'_r \cdot \boldsymbol{e}_1^{(r)}\right)^2 j_{\nu,1} + \left(\boldsymbol{y}'_r \cdot \boldsymbol{e}_2^{(r)}\right)^2 j_{\nu,2}, \quad (6)$$

where the quantities $\boldsymbol{x}'_r \cdot \boldsymbol{e}_\ell^{(r)}$ and $\boldsymbol{y}'_r \cdot \boldsymbol{e}_\ell^{(r)}$ are given in appendix B of Potekhin et al. (2012).[5] We note that equations (6) hold if $j_{\nu,1}$ and $j_{\nu,2}$ are mutually incoherent. Actually, under the conditions considered in this work, the differences introduced by applying the complete transformation of Potekhin et al. (2012) are negligible (except possibly at 10 keV), as we checked numerically. The corresponding intensities are then expressed as

$$I_{\nu,O} = j_{\nu,O}(B, \nu, \theta_B, \theta_k, \phi_k) B_\nu(T)/2$$

$$I_{\nu,X} = j_{\nu,X}(B, \nu, \theta_B, \theta_k, \phi_k) B_\nu(T)/2, \quad (7)$$

Following van Adelsberg et al. (2005, see also Potekhin et al. 2012), our calculations are performed in the simplifying limits of free and fixed ions. As already noted by van Adelsberg et al. (2005), a more realistic description of the actual reflectivity can be expected to lie

---

[5]Note that a typo is present in equation (B.12) of Potekhin et al. (2012), where $\cos^2\theta_k - \sin^2\theta_k$ should be $\cos^2\theta_k + \sin^2\theta_k$. The correct expression can be found in arXiv:1208.6582.

in between the previous limits. Finally we warn that, as for the atmosphere model discussed above, also in this case no allowance for the effects of returning currents is made.

3 NUMERICAL IMPLEMENTATION

The present investigation relies on the Monte carlo code developed by Nobili et al. (2008) for simulating the persistent emission from magnetar sources in the framework of the RCS model. The polarization observables (linear polarization degree and angle) are computed accounting for the evolution of polarization states in the magnetized vacuum (vacuum birefringence) by a specific module (see Taverna et al. 2014, for further details). We assumed a globally twisted dipole field, characterized by the polar strength B_p and the radial index p,

$$\boldsymbol{B} = \left(B_r, B_\theta, B_\phi\right)$$

$$= \frac{B_p}{2}\left(\frac{r}{R_{NS}}\right)^{-p-2}\left[-f', \frac{pf}{\sin\theta}, \sqrt{\frac{C(p)\,p}{p+1}}\frac{f^{1+1/p}}{\sin\theta}\right], \quad (8)$$

where the angular part of the flux function $f(\mu)$ satisfies the Grad–Schlüter–Shafranov equation

$$(1-\mu^2)f'' + p(p+1)f + Cf^{1+2/p} = 0; \quad (9)$$

here $\mu = \cos\theta$, a prime denotes the derivative wrt μ and the constant C is an eigenvalue (Thompson et al. 2002; Pavan et al. 2009). We remark that globally twisted dipole fields are a particular case of the much more general force-free equilibria, obtained by adding a defined amount of shear to the (potential) dipole field. The shear itself is expressed in terms of p or, more conveniently, through the twist angle $\Delta\phi_{N-S}$,

$$\Delta\phi_{N-S} = \lim_{\theta_0 \to 0} 2\int_{\theta_0}^{\pi/2} \frac{B_\phi}{B_\theta}\frac{d\theta}{\sin\theta}, \quad (10)$$

which measures the amount of angular displacement suffered by a field line in going from the north to the south magnetic pole.

Charges are assumed to flow along the closed field lines with constant velocity β (in units of the speed of light). We retain the original hypothesis introduced in Fernández & Thompson (2007, see also Nobili et al. 2008) of an unidirectional flow of electrons, streaming from the north to the south magnetic hemisphere (see Section 6 for further details).

Emission from the star is handled by dividing the surface into a number of equal-area patches by means of a Θ_s–Φ_s grid, where Θ_s is the magnetic colatitude and Φ_s the azimuth of the patch centre. Photons are eventually collected on to a sphere representing the observer's sky (see Nobili et al. 2008, for further details). In the

actual calculations a 10×10 and a 20×10 angular meshes were used in the case of condensed surface and atmosphere models,[6] respectively, while a 15×15 grid was adopted for the sky-at-infinity in all cases. The number of seed photons is arbitrarily fixed for a reference patch and follows from the scaling with the number flux for the remaining ones (e.g. T^3 in the case of blackbody emission).[7] In the original version of the code, a blackbody photon distribution at the local temperature T was assumed, together with the linear polarization fraction (either 100 per cent polarized in the X- or O-mode, or unpolarized, i.e. 50 per cent X and 50 per cent O). Now instead, the polarization degree of the emitted radiation consistently follows once the surface emission model is specified. No allowance for general relativistic (GR) effects is made in the calculations, mostly to avoid an undue increase in computational time when running a large number of Monte carlo simulations. This is tantamount to ignore light bending and gravitational redshift. GR light bending outside an NS (assuming a Schwarzschild space–time) exposes a larger part of the star surface to a faraway observer (actually, for typical values of the NS mass and radius, more than 2/3 of the entire surface will be visible at the same time). This deeply impacts e.g. on the observed pulsed fraction for surface emission from cooling, isolated NSs (see e.g. Beloborodov 2002; Turolla & Nobili 2013). In the case of magnetar sources, where RCS is at work, the effects are likely less important, because a sizable part of the radiation emitted by the surface will scatter at ∼5–10 star radii, where GR effects already abated, before reaching infinity. Results obtained with Monte carlo codes including or not GR ray-tracing are, in fact, in good agreement (Fernández & Davis 2011; Taverna et al. 2014). Strong gravity can also influence the photon polarization state, because of the rotation of the polarization plane along the null geodesics (Connors & Stark 1977; Stark & Connors 1977; Connors, Piran & Stark 1980). However, the typical scale length over which vacuum birefringence acts is much shorter than that of gravity, so that the effects of the latter on polarization are negligible around ultra-magnetized NSs.

3.1 Sampling the seed photon distribution

The starting point of the Monte carlo simulation is to generate seed photons randomly distributed according to the specific intensity of the radiation emitted from the star surface. Obtaining a random deviate from a Planckian distribution poses in general no difficulties on a numerical ground, since an efficient method can be devised despite the fact that the associated cumulative density function (cdf) is not analytically invertible. On the other hand, generating a random deviate in the case of emission from a condensed surface or a magnetized atmosphere requires a greater computational effort. A simple way of dealing with this is using the acceptance/rejection method (von Neumann 1951; Press et al. 1992), which can be exploited in those cases in which a random variable has to be generated from a probability density function (pdf) f with non-invertible (or not even computable) cdf. The key point is to find a function g (the majorizing function) such that $g > f$ in the desired range and from which a random deviate can be easily obtained. Once a random variable x is extracted from the normalized majorizing

distribution $\bar{g}$, the ratio $h(x) = f(x)/g(x)$ is calculated and, if the condition $y < h(x)$ (with y an uniform random deviate between 0 and 1) is met, then x provides a sampling of the starting pdf f.

In the case at hand, the anisotropic emission of both the atmosphere and the condensed surface requires an extension of the acceptance/rejection technique to three dimensions: the photon frequency ν and the two angles θ_k and ϕ_k (or η and ψ) which fix the photon direction. This can be addressed by choosing a majorizing function $g_{\nu,j}$ independent of the angles and such that $g_{\nu,j} > I_{\nu,j}(\theta_k, \phi_k)$ for any value of θ_k and ϕ_k ($j = $ O, X). In this way the photon energy is generated according to the distribution $I_{\nu,j}$, while the two angles are extracted from uniform deviates, in the ranges $0 \le \eta \le \pi$ and $0 \le \psi \le \pi$ for the atmosphere model, and $0 \le \theta_k \le \pi/2$ and $0 \le \phi_k \le 2\pi$ for the condensed surface one.[8] Care must be taken that $g_{\nu,j}$ is as close as possible to $I_{\nu,j}$, in order for the rejection method to be efficient. We found that a Planckian shape for $g_{\nu,j}$ with a suitable scaling works well in all cases. This choice has also the advantage that our Monte carlo code already contains an algorithm to generate random deviates from a normalized Planckian distribution. This ensures that photons are emitted with the correct angular distribution, as we numerically tested. For the atmosphere model, in which the intensities are tabulated, a three-dimensional, linear interpolation is performed in order to evaluate I_ν at the required photon energies and angles.

3.2 Polarization mode evolution

In order to determine the initial polarization state of each emitted photon, the code numerically integrates the specific intensity to get, for each surface patch, the ratio J_X/J, where J (J_X) is the grey total (X-mode) mean intensity. For each emitted photon an uniform random deviate U is then generated: the photon is labelled as extraordinary if $U < J_X/J$ and as ordinary otherwise.

Since the typical densities in magnetar magnetospheres are $\approx 10^{16}$ cm^{-3}, polarization transport is dominated by the dielectric and magnetic permeability properties of the magnetized vacuum, as it follows from the equation of plane waves (see e.g. Harding & Lai 2006, and references therein). Closer to the star surface, where the magnetic field is stronger, the effect of magnetized vacuum is to lock the photon polarization vector to the local magnetic field direction (adiabatic region). As radiation propagates outwards, the polarization vector progressively decouples (intermediate region) until, at large distances, it freezes (external region). Since under typical magnetar conditions RCS occurs well inside the adiabatic region, in the Monte carlo code the calculation of the Stokes parameter evolution starts once the escape condition is met, i.e. when the probability for photons to undergo further resonant scatterings has sufficiently dropped (Fernández & Davis 2011; Taverna et al. 2014). First the Stokes parameters are rotated, so as to express them in a (common) fixed frame; then the integration of the evolution equations is performed until a large enough radius is reached. Some improvements over the original treatment were introduced. In particular, care has been taken in selecting the starting point for the Stokes parameter evolution always inside the adiabatic

---

[6]The latter is given in Table 1 for the Northern hemisphere (the patches in the Southern hemisphere are obtained by mirroring with respect to the magnetic equator).

[7]The reference patch is actually chosen as the one which emits the lowest number of photons.

[8]In the atmosphere case, some values of (η, ψ) may actually label incoming rays, i.e. the corresponding value of θ_k, as derived from the first of equations (1), turns out to be $> \pi/2$. When this happens, symmetry considerations allow to associate the intensity $I_\nu(\eta, \psi)$ to the direction characterized by the angles $\pi - \theta_k$ and $\pi + \phi_k$.
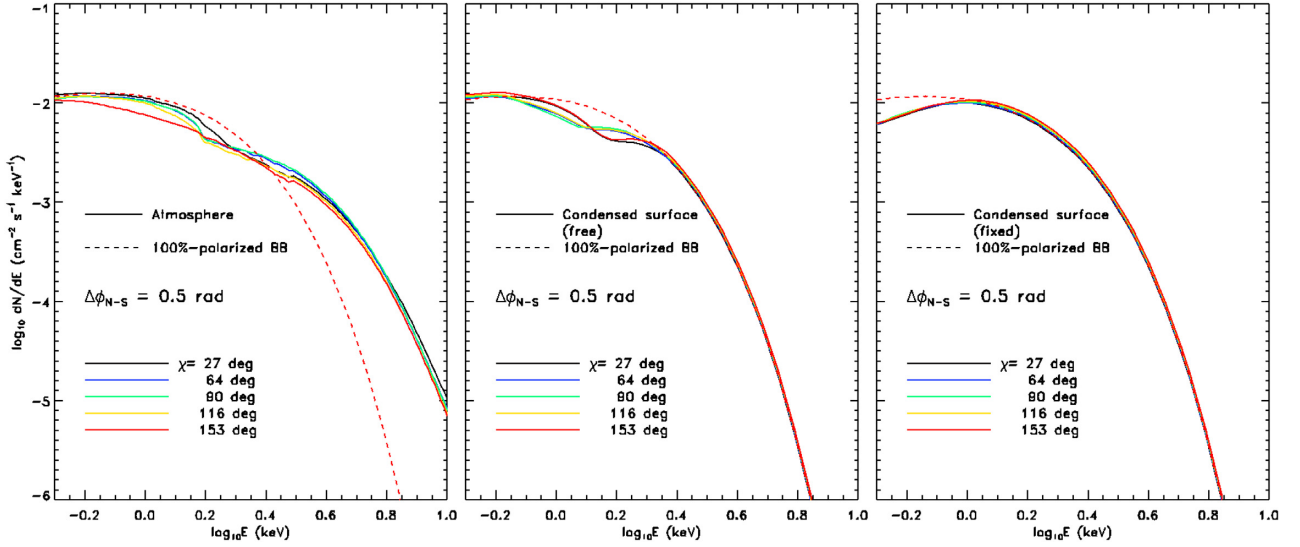
Figure 4. Number flux as a function of the photon energy for the atmosphere (left) and condensed surface models (free-ion middle, fixed-ion right) as seen by an observer at infinity. Here the external magnetic field is a globally twisted dipole with $B_p = 5 \times 10^{14}$ G and $\Delta\phi_{N-S} = 0.5$ rad. The star is an aligned rotator ($\xi = 0$) seen at different inclinations χ. The dashed lines show the 100 per cent polarized blackbody spectrum for the same values of the parameters. Here, no effects from magnetospheric scatterings are accounted for (see text for details).

region, to correctly handle also low-energy photons which never scatter.[9]

4 RESULTS

In the following we present Monte carlo simulations of magnetar persistent emission both in the case of a condensed surface (in the free/fixed ion limits) and of a magnetized hydrogen atmosphere. In particular we highlight the similarities and differences with respect to previous results obtained for blackbody surface emission 100 per cent polarized (see Nobili et al. 2008; Fernández & Davis 2011; Taverna et al. 2014). We remark that this does not correspond to any physical situation but provides a simple way to investigate how the polarization of (thermal) photons emitted by the surface is influenced by magnetospheric RCS and QED effects before reaching the observer. All models have been computed assuming a unidirectional (electron) flow, for a polar magnetic field strength $B_p = 5 \times 10^{14}$ G and a (homogeneous) surface temperature $kT = 0.5$ keV. These values are representative of magnetar sources (Olausen & Kaspi 2014; Kaspi & Beloborodov 2017) and close to those inferred for the AXPs 1RXS J170849.0−400910 (in the following J1708, $B_p = 9 \times 10^{14}$ G, $T = 0.5$ keV; see Rea et al. 2007a; Dib & Kaspi 2014) and 4U 0142+61 ($B_p = 3 \times 10^{14}$ G, $T = 0.4$ keV; see Rea et al. 2007b), two selected targets for polarimetric measurements with *IXPE* (see Section 5). The velocity spread of magnetospheric electrons is accounted for assuming a 1D Maxwellian distribution with temperature $kT_e = 10$ keV. The charge density along the closed field lines is given by

$$n_e \sim 3 \times 10^{15} \left(\frac{B_\phi}{B_\theta} \right) \left(\frac{B}{10^{13}\,\mathrm{G}} \right) \left(\frac{r}{10^6\,\mathrm{cm}} \right)^{-1} |\langle\beta\rangle|^{-1}\,\mathrm{cm}^{-3}, \quad (11)$$

where r is the radial distance and $\langle\beta\rangle$ the average charge speed (arising from the superposition of bulk and thermal motions; see e.g. Thompson et al. 2002; Nobili et al. 2008). All runs were

performed emitting 80 000 photons from the reference patch (40 000 for the atmosphere model), so that the total number of photons is about 10^7.

We produced a set of models varying the two free parameters $\Delta\phi_{N-S}$ and β in the ranges [0.3, 1.4] rad (step 0.1) and [0.2, 0.7] (step 0.1, with the addition of $\beta = 0.34$), respectively. Such an archive of models will be useful especially for polarimetry simulations (see Section 4.2). The source geometry is characterized by the two angles χ and ξ that the rotation axis makes with the observer's line of sight (LOS) and the star magnetic axis, respectively. Geometric effects are then incorporated at the post-processing level using a suite of IDL codes (see Nobili et al. 2008; Taverna et al. 2014).

4.1 Spectra

In order to better understand the effects of RCS on the surface emission, we start reporting in Fig. 4 the spectra of primary photons, i.e. assuming no reprocessing in the magnetosphere, as measured by an observer at infinity, accounting for emission from the entire star surface for each of the three models considered. Spectral (and polarimetric, see Fig. 8) calculations were performed using the ray-tracing code discussed in Taverna et al. (2015, see also Zane & Turolla 2006). Here the star is an aligned rotator, and the different solid curves refer to different inclinations of the LOS; results for 100 per cent polarized, blackbody seed photons are also shown for comparison (dashed lines). The external magnetic field is a globally twisted dipole with $\Delta\phi_{N-S} = 0.5$ rad and $B_p = 5 \times 10^{14}$ G. The atmospheric model shows the characteristic hardening with respect to the blackbody at $E \gtrsim kT = 0.5$ keV and blending of the proton cyclotron line (which occurs at different energies since B changes from patch to patch, see e.g. Fig. 3) produces a broad depression around $\sim$2 keV. Following Ho, Potekhin & Chabrier (2008), to avoid numerical oscillations in the $\approx$1.5–3 keV range, the specific intensities have been re-interpolated over a E/E_{Bp} grid (with E_{Bp} the proton cyclotron energy) before integrating over the visible part of the star surface. Condensed surface spectra are closer to the blackbody, although an absorption feature appears in the free-ions

---

[9]We note that this is not going to produce any effect at X-ray energies, while it is potentially important in the optical range.
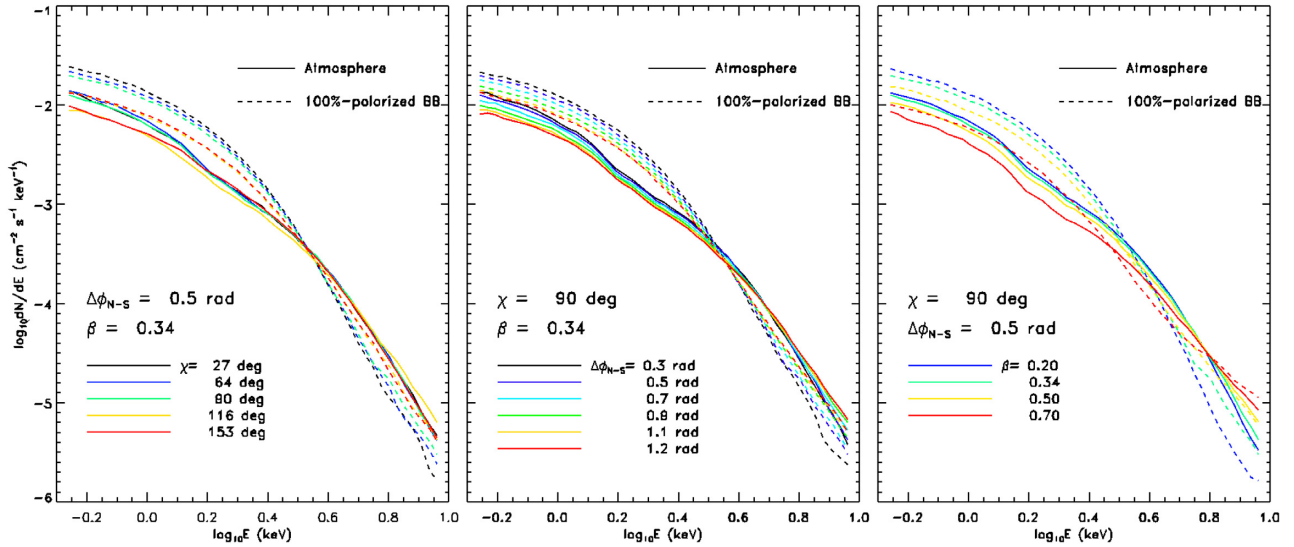
Figure 5. Number flux as a function of the photon energy computed in the case of emission from a magnetized, partially ionized H atmosphere (solid lines). The plots refer to an aligned rotator ($\xi = 0$) with polar magnetic field $B_p = 5 \times 10^{14}$ G (see text for more details). The left-hand, middle, and right-hand panels show spectra for different values of the LOS inclination (χ), the twist angle ($\Delta\phi_{N-S}$) and the electron velocity (β), respectively. Spectra for the same values of the parameters but in the case of 100 per cent polarized blackbody seed photons are also shown (dashed lines) for comparison.
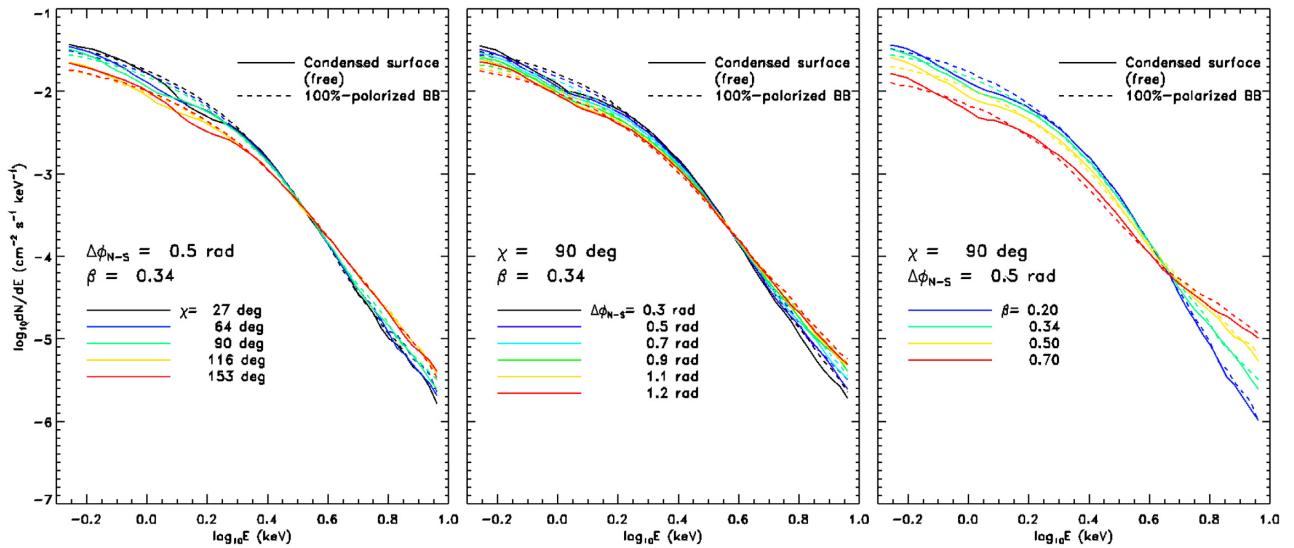
Figure 6. Same as in Fig. 5 but for condensed surface emission in the free-ion limit.

case and the distinct low-energy cut-off is visible in the fixed-ions limit.

The number flux as a function of the photon energy in the full case in which also RCS is included is plotted, instead, in Fig. 5 for the atmosphere model, and in Figs 6 and 7 for the condensed surface one in the free- and fixed-ion limits, respectively. The star is still an aligned rotator ($\xi = 0$), and the different solid curves correspond to different values of the LOS inclination χ (left), twist angle $\Delta\phi_{N-S}$ (middle), and electron velocity β (right). The same spectra but for 100 per cent polarized blackbody seed photons are also shown for comparison (dashed lines). In this latter case, as discussed in detail by Fernández & Thompson (2007) and Nobili et al. (2008), spectra exhibit a distinctive 'blackbody + power-law' behaviour in the 0.5–10 keV energy range, with the spectral hardness increasing for increasing values of $\Delta\phi_{N-S}$ and β, as it can

be clearly seen from the dashed lines of Figs 5–7. When considering different surface emission models, the overall spectral shape turns out to still follow a 'thermal + power-law' behaviour. Deviations with respect to the 100 per cent polarized blackbody case however appear and are especially evident in the low-energy range (0.5–2 keV), where the primary photon distributions peak and hence a larger fraction of photons reaches infinity without undergoing scatterings. In the light of this, such deviations with respect to the 100 per cent polarized blackbody clearly reflect the intrinsic differences among the considered surface emission models, that are particularly pronounced in the case of atmospheric seed photons (Fig. 5), where the imprint of the broad absorption line is visible at few keVs. Smaller differences are also present in the case of free ions (Fig. 6), with the appearance of an 'absorption feature' at around 1.2 keV, intrinsic to the emissivity distribution and related
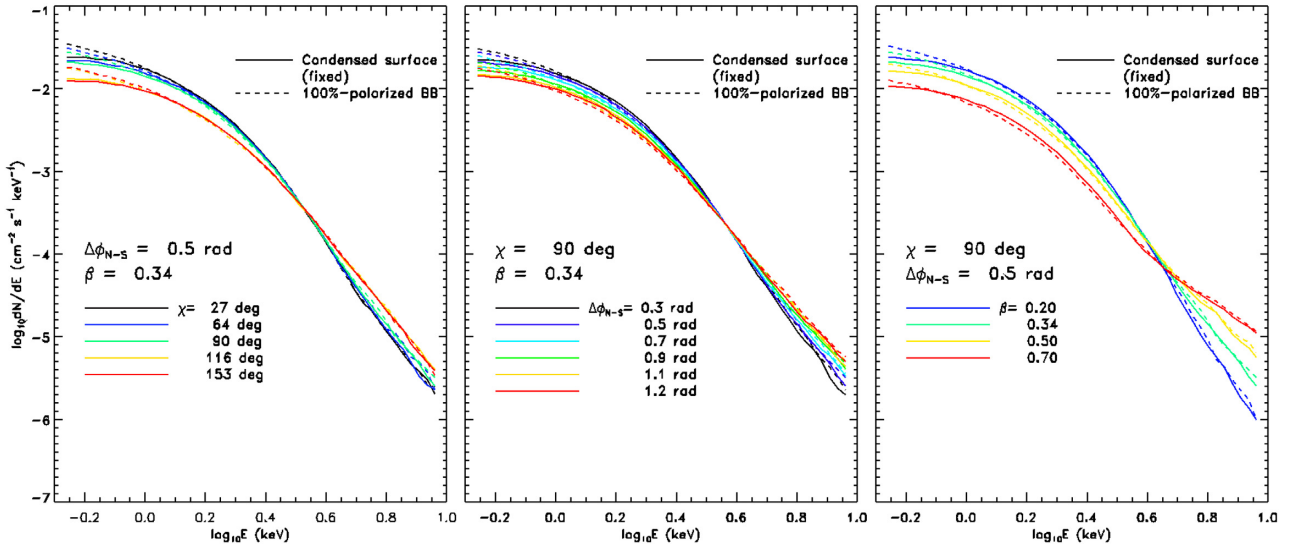
Figure 7. Same as in Fig. 5, but for condensed surface emission in the fixed-ion limit.

to the proton cyclotron resonance and electron plasma frequency (see van Adelsberg et al. 2005; Potekhin et al. 2012).

On the other hand, not unexpectedly, the power-law tails are little affected by the details of the seed photon distribution, so that the spectral indices, which depend only on the magnetospheric parameters, turn out to be quite the same for all the considered models. However, at high energies some differences appear. In fact, for the condensed surface the power-law tails develop at lower energies (∼3 keV), much as in the blackbody case, while for the atmosphere this occurs only above ∼5 keV, as expected since the seed photon distribution is harder (see left-hand panel of Fig. 4).

4.2 Polarization

As in our discussion of RCS spectra, we first introduce the polarization properties of surface thermal radiation, calculated following the same approach outlined in González Caniulef et al. (2016), since this will help in disentangling the effects produced by resonant scattering from those intrinsic to surface emission. Fig. 8 shows the energy-dependent polarization fraction Π_L measured at infinity for the atmosphere and condensed surface models. Vacuum birefringence is included, while GR effects are ignored for consistency with the Monte carlo calculation. Atmospheric emission turns out to be strongly polarized (≈80–100 per cent) over the entire considered energy band. On the other hand, Π_L is substantially reduced for the condensed surface with respect to both the blackbody and the atmosphere cases, generally attaining a value smaller than 20 per cent. In particular, local minima (where $\Pi_L \sim 0$) occur at different photon energies, according to the different geometry considered. Looking at the polarization angle behaviour (not shown here, but see the bottom-right panel of Fig. 12 for the general picture), these minima correspond to energies at which the dominant photon polarization state switches from one normal mode to the other.

The complete RCS results are reported in Figs 9, 10, and 11, following the same scheme discussed Section 4.1. Comparing the left-hand panels with the plots shown in Fig. 8, it can be noted that the behaviour of Π_L below ∼4 keV bears the imprint of the different intrinsic polarization patterns. On the other hand, the polarization degree dramatically changes with respect to the intrinsic one in

the high-energy tail (≳ 5 keV), where scattering effects become dominant. RCS acts in depolarizing radiation in the atmosphere case, much in the same way as in the case of 100 per cent blackbody radiation, since X-mode seed photons are progressively converted into O-mode ones by scattering (with 33 per cent chance, see Nobili et al. 2008). The opposite occurs, instead, for photons emitted by the condensed surface, which acquire more and more polarization as they scatter in the star magnetosphere.[10] In particular, for all the different emission models considered, the polarization degree reaches a value ≈20–40 per cent, in agreement with the expected saturation value, 33 per cent, imposed by the ratio between the X- and O-mode RCS scattering cross-sections.
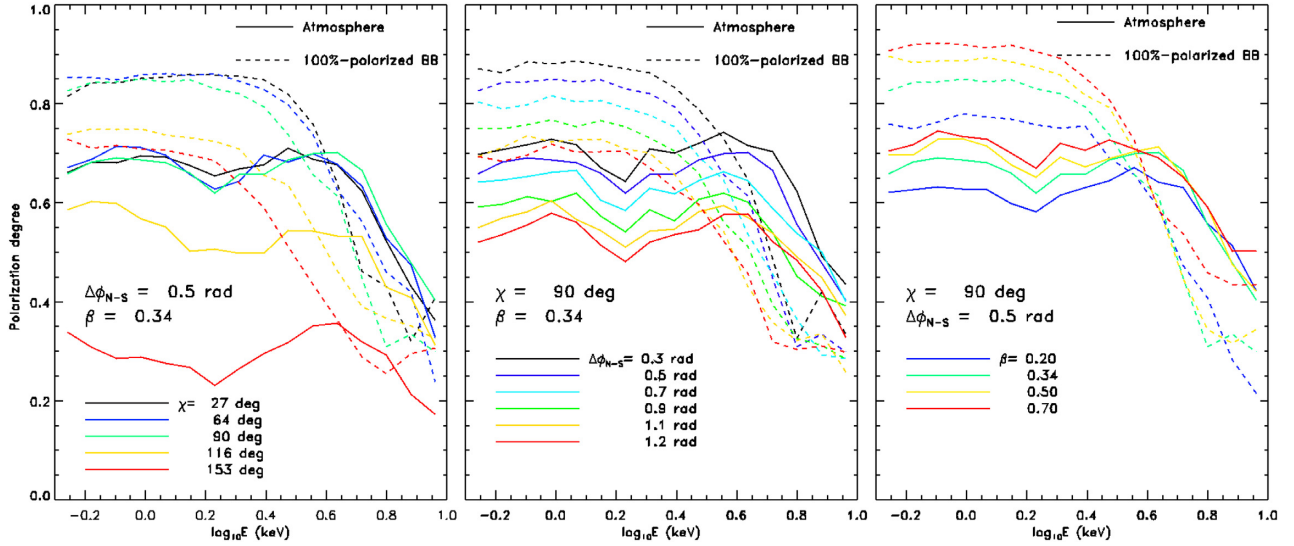
The polarization degree as a function of the photon energy in the magnetized atmosphere case (see Fig. 9) is fairly constant al low energies (≲ 4 keV), exhibiting only a modest decrease in correspondence to the proton absorption feature of the primary spectrum. It then declines at higher energies, although it is somehow higher than in the blackbody case for the different configurations. This trend, which may appear quite surprising since blackbody photons are 100 per cent polarized in the X-mode, can be understood noticing that atmospheric spectra are harder than a blackbody (see Section 4.1) and that the intrinsic polarization still approaches 100 per cent at high energies (see Fig. 8, left-hand panel). As mentioned discussing the spectra, while in the case of blackbody emission the power-law tail is predominantly populated by low-energy, up-scattered seed photons, there is a still important fraction of highly polarized seed photons around ≈3–4 keV in the atmosphere case, which mitigates the effects of RCS maintaining the overall polarization degree relatively large, before it decreases above ≈5 keV.

The trends of Π_L as a function of the model parameters exhibited in Figs 9–11 can be understood as follows. Concerning the LOS inclination (left-hand panels), we note that in the blackbody case Π_L generally decreases by increasing χ. This is due to the fact that particles are assumed to stream from the north to the south magnetic

---

[10]The rise in Π_L at higher energies may be also due to a marginal increase in the intrinsic polarization fraction, as it can be seen in the middle and right-hand panels of Fig. 8.
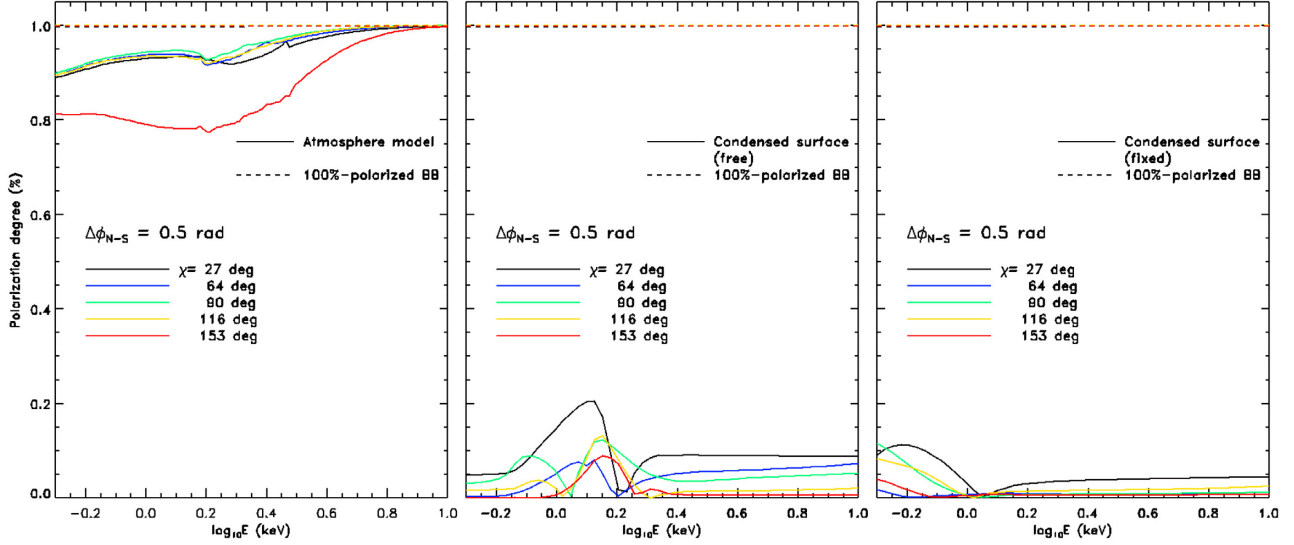
Figure 8. Linear polarization degree as a function of the photon energy of the surface radiation for the atmosphere (left), condensed surface free-ion (middle) and fixed-ion (right) models as seen by an observer at infinity. Here the external magnetic field is a globally twisted dipole with $B_p = 5 \times 10^{14}$ G and $\Delta\phi_{N-S}$ = 0.5 rad. The star is an aligned rotator ($\xi = 0$) seen at different inclinations χ. The dashed lines show the intrinsic polarization for the same values of the parameters for blackbody, 100 per cent polarized seed photons. Here, no effects from magnetospheric scatterings are accounted for (see text for details).

Figure 9. Linear polarization degree as a function of the photon energy computed in the case of a magnetized, partially ionized H atmosphere (solid lines). Details as in Figs 5–7.

pole (unidirectional flow), so that in the Southern hemisphere scatterings are mostly head-on, resulting in a larger cross-section. The same effect is responsible for the hardening of the spectrum at high energies seen in the left-hand panels of Figs 5, 6, and 7 (see also Nobili et al. 2008). This also shows that the 0.2–2 keV range contains photons that indeed scatter but without a substantial change in their energy (and in fact the spectral shape is unchanged, see Fig. 5), together with unscattered, primary ones. In this respect, we note that the way RCS polarizes radiation is different from that of non-magnetic Thomson scattering in which geometry plays a fundamental role. The decrease of Π_L with χ is less prominent in the condensed surface case, since at low energies the intrinsic polarization is small, becoming sizeable only above ~5 keV, where up-scattered photons dominate. Actually, in the 2–4 keV energy range the trend may be even reversed, with the polarization degree

consistently higher for $\chi > 90°$ than for the other directions. At these intermediate energies, in fact, the polarizing effect of RCS starts to be evident as soon as the Southern hemisphere is in view (see also the discussion of Fig. 12 below). In a similar way, the change of the polarization degree with $\Delta\phi_{N-S}$ and β (see middle and right-hand panels, respectively) is related to the form of the RCS optical depth, which roughly goes as $\sim\Delta\phi_{N-S}/\beta$ (Fernández & Thompson 2007; Nobili et al. 2008). In fact, in the blackbody case Π_L decreases by increasing $\Delta\phi_{N-S}$ and decreasing β. In the condensed surface case, instead, this is mirrored only at higher energies, where the polarization degree is large enough to make the effect visible.

The behaviour of the polarization degree and angle (χ_{pol}) as functions of the photon energy and the rotational phase γ is illustrated in Fig. 12 for 100 per cent polarized blackbody (left
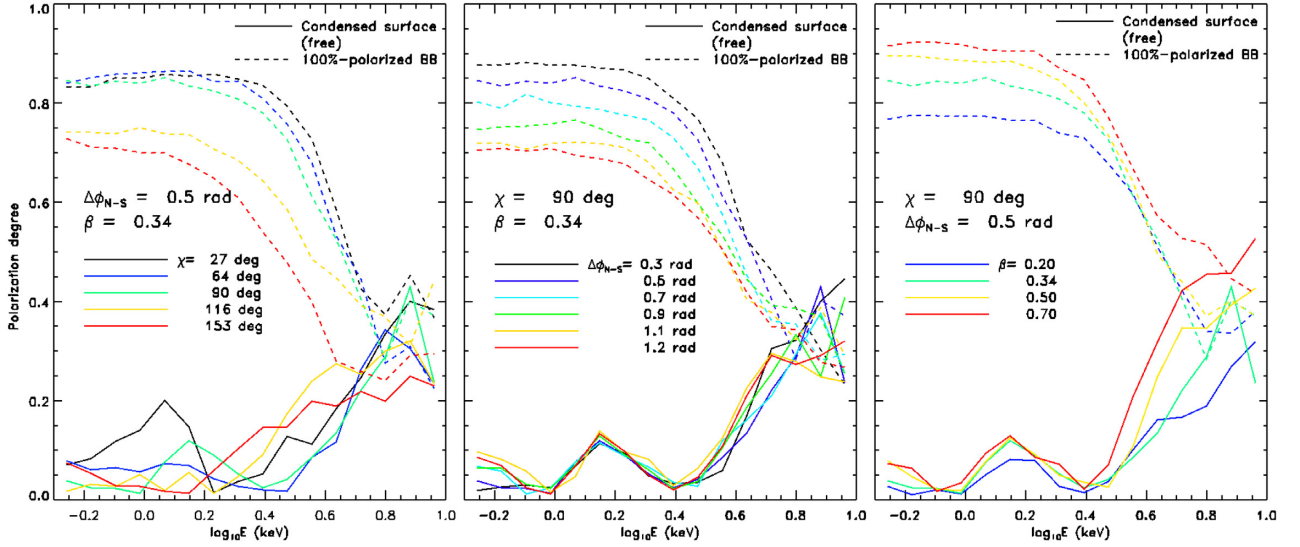
Figure 10. Same as in Fig. 9, but in the case of condensed surface emission in the free-ion limit.
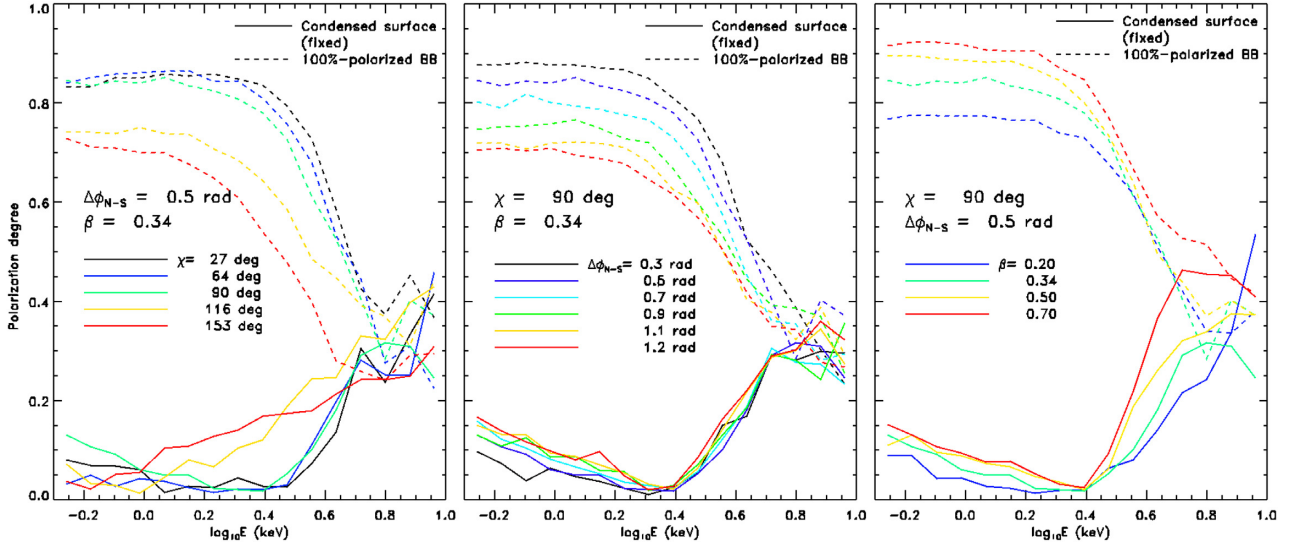

Figure 11. Same as in Fig. 9, but in the case of condensed surface emission in the fixed-ion limit.

column), atmosphere (middle column) and condensed surface (free-ions, right column) models. Here the magnetic axis and the observer's LOS are at $\xi = 60°$ and $\chi = 90°$ with respect to the star rotational axis; the model parameters are fixed at $\Delta\phi_{N-S} = 0.5$ rad and $\beta = 0.34$. The variation of Π_L with the rotational phase can be explained taking into account that surface patches at different magnetic colatitudes θ enter into view as the star rotates, since θ varies with γ according to $\cos\theta = \cos\chi\cos\xi + \sin\chi\sin\xi\cos\gamma$ (see e.g. Taverna et al. 2014, in particular $30° \lesssim \theta \lesssim 150°$ for the case at hand). For 100 per cent polarized blackbody radiation (top-left panel), the polarization degree at low photon energies turns out to be as high as ~ 80 per cent for $-\pi/2 \lesssim \gamma \lesssim \pi/2$ (when $30° \lesssim \theta \lesssim 90°$), while it drops to ~ 60 per cent at $\gamma \sim \pi$, which corresponds to $\theta \sim 150°$. This is tantamount to say that the northern (magnetic) hemisphere is in view in the former configuration, whereas the southern one is visible in the latter. As discussed above (see the left-hand panels of Figs 9–11), a higher polarization degree

is expected when the northern magnetic pole enters into view. On the contrary, at high energies ($\gtrsim 3$ keV), where scattering effects are more significant (see the left-hand panels in Figs 5–7), the polarization fraction is below ≈ 50 per cent and quite independent of the rotational phase (despite the low statistics introduces some noise at these energies).

The behaviour of the polarization fraction and angle in the case of a magnetized atmosphere (middle column) follows closely that of the blackbody although, as discussed earlier on, the polarization fraction is somewhat higher at higher energies and lower around the absorption feature. For the condensed surface model (right column) the polarization fraction at low photon energies is quite small ($\lesssim 10$ per cent), with in general a fairly weak dependence on the rotational phase. The only exception occurs in the 2–4 keV energy range, where Π_L increases for $0 < \gamma < \pi$, attains a maximum (≈ 30 per cent) at $\gamma \approx \pi$ and then decreases again for $\pi \lesssim \gamma \lesssim 2\pi$. This peculiar trend can be again explained as an effect of RCS that,
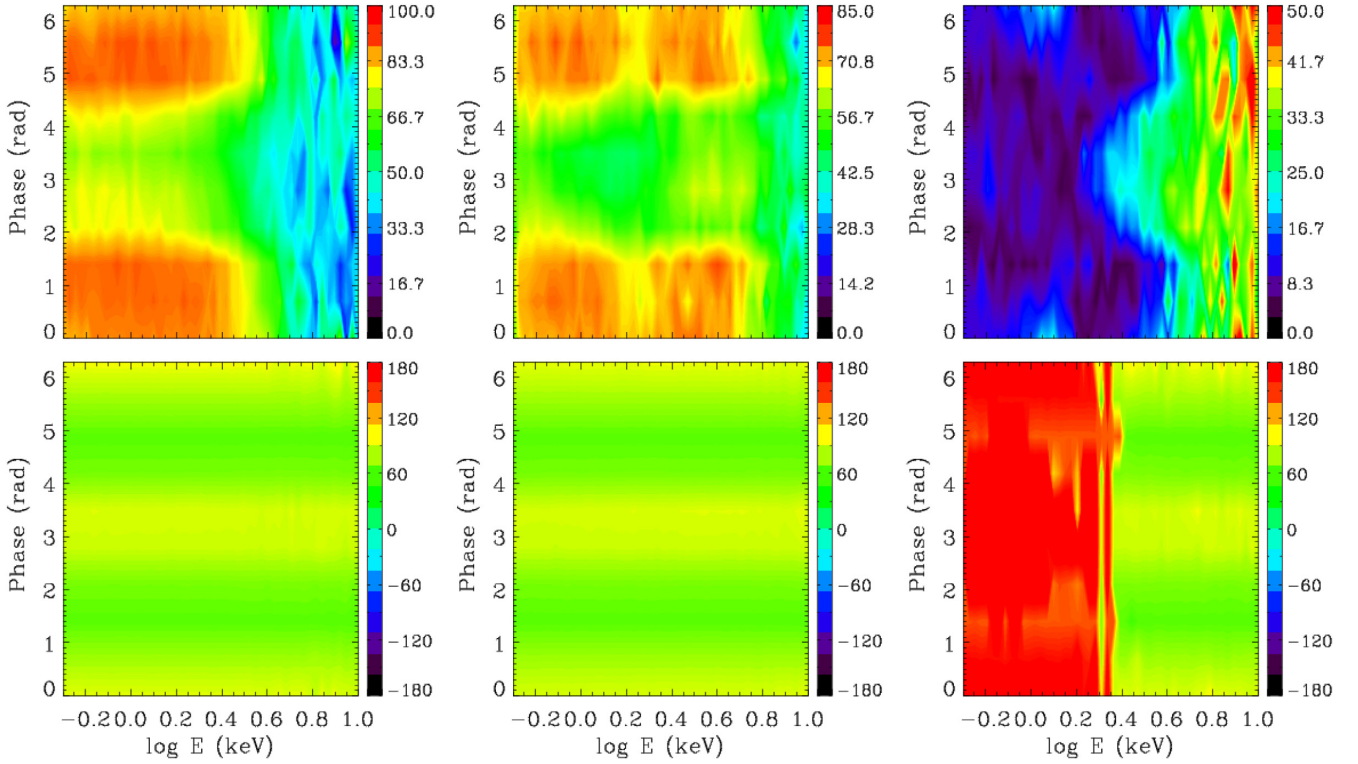
Figure 12. Linear polarization degree (top row) and polarization angle (bottom row) as functions of photon energy and rotational phase for the blackbody (100 per cent polarized seed photons, left), atmosphere (middle) and condensed surface (free-ion limit, right). Note the different colour scales for the polarization degree. The plots refer to $B_p = 5 \times 10^{14}$ G, $\Delta\phi_{N-S} = 0.5$ rad, $\beta = 0.34$, $\chi = 90°$, and $\xi = 60°$.

as mentioned above, tends in general to polarize radiation in the condensed surface case. In fact, the increase in Π_L due to scatterings becomes sizeable precisely around these energies, starting at those phases ($\gamma \approx \pi$) at which the southern magnetic hemisphere, where RCS is more efficient, enters into view (see also the discussion of Figs 10 and 11 above). At higher energies the polarization degree settles down to ≈ 30–40 per cent without an evident variation with the rotational phase.

The polarization properties for the condensed surface model just discussed are further confirmed by the behaviour of polarization angle (bottom-right panel). The latter is characterized by two distinct regimes: at low photon energies ($\lesssim 2$ keV), χ_{pol} is nearly constant at $\sim 180°$ over the entire phase interval, which is compatible with a larger fraction of O-mode photons; at higher energies ($\gtrsim 2$ keV), it oscillates around an average value $\sim 90°$, due to a predominance of X-mode photons (see e.g. Taverna et al. 2015). The fact that X-mode photons become dominant starting at 2–4 keV, precisely where the increase of Π_L occurs, is again due to the effect of RCS, since scatterings drive an increase of X-mode photons with respect to O-mode ones (as already noted by Nobili et al. 2008). On the other hand, the polarization angle for both the blackbody (bottom-left panel) and the atmosphere (bottom-middle panel) models resembles in the entire energy range the trend exhibited at high energies for the condensed surface case, with an overall predominance of extraordinary photons. Whilst in the blackbody case this is produced by the choice of 100 per cent polarized seed photons in the X-mode, in the atmosphere one it reflects the intrinsic properties of radiative processes in the presence of strong magnetic fields, with X-mode opacities much reduced with respect to O-mode ones.

5 SIMULATING OBSERVATIONS WITH *IXPE*

Despite polarization measurements are unanimously recognized as a key tool in modern astrophysics and are routinely used in different bands of the electromagnetic spectrum, no dedicated space mission for X-ray polarimetry ever flew. Since the pioneering time of *OSO-8* (Weisskopf et al. 1978), polarimetric measures at X-rays relied only on rocket and balloon experiments (see Bellazzini et al. 2010; Weisskopf 2018, for an overview), with the exception of the small GPD detector *PolarLight* (Feng et al. 2019), which flew in 2018 on board of the CubeSat satellite. Only recently, with the development of photoelectric polarimeters (Costa et al. 2001), the interest in X-ray polarimetric observatories was revived. This led to a number of proposals, including the NASA *GEMS* (Baumgartner et al. 2012) and *PRAXyS* (Jahoda et al. 2014), and the ESA *XIPE* (Soffitta et al. 2016), which however were not selected. Nowadays, two promising missions are looming on the horizon: the *IXPE* mission (Weisskopf et al. 2016), selected for the NASA SMEX programme and scheduled for launch in early 2021; and the *eXTP* mission (Zhang et al. 2019; Santangelo et al. 2019b), which has been approved by the Chinese Academy of Science, and is expected to fly in 2025.

Magnetars are among the key science targets of *IXPE* and *eXTP*, especially in connection with the possibility to test birefringence in the ultra-magnetized vacuum around NSs (Santangelo et al. 2019a). On the wake of the results discussed in Taverna et al. (2014), here we present a set of simulated *IXPE* observations meant to be representative of the bright AXPs 1RXS J170849.0−400910 and 4U 0142+61, which have been selected for the first year of operations. The model parameters are $\Delta\phi_{N-S} = 0.5$ rad, $\beta = 0.34$

and $T = 0.5$ keV (constant over the surface), i.e. the same derived from the RCS spectral fitting of J1708 (Zane et al. 2009), and $B_p = 5 \times 10^{14}$ G. The different flux level of the two sources is accounted for by rescaling the Monte carlo output in such a way to produce a 2–10 keV unabsorbed flux of 2.4 (6.8) $\times 10^{-11}$ erg cm^{-2} s^{-1} (see again Olausen & Kaspi 2014).

Phase-dependent simulations for the flux, linear polarization fraction and angle were produced using a specific code (see e.g. Taverna et al. 2014, for more information) which incorporates *IXPE* instrumental set-up (modulation factor and effective area according to the most updated release). The phase bins were selected in such a way to ensure that each bin contains a large enough number of counts. In the case of J1708 (4U 0142+61) we checked that, with 9 bins, about 5 (13) photons are collected in any phase interval. For each simulated observation, we performed $N \sim 100$ realizations based on the same input model ($\chi = 90°$, $\xi = 60°$, $\Delta\phi_{N-S} = 0.5$, $\beta = 0.34$). The flux, polarization degree and angle derived from each of these were simultaneously fitted using an archive of models obtained varying the parameters; the one with the median reduced χ^2 is finally selected.

Fig. 13 illustrates the results for 100 per cent polarized blackbody (top row), atmosphere (middle row), and condensed surface (fixed-ions,[11] bottom row) emission models. Simulated data refer to the 2–8 keV energy range for both the blackbody and atmosphere, and to the 4–8 keV range for the condensed surface, for which the contribution to Π_L between 2 and 4 keV is small (see Fig. 11). An exposure time $t_{exp} = 500$ ks is assumed, apart from the condensed surface model, for which $t_{exp} = 1$ Ms. The orange solid line represents the model from which the mock data were generated, while the green solid line corresponds to the best-fitting model. In all cases the fit recovers the input parameters with good accuracy (within 1σ, see Table 2). The dashed orange line shows instead the input model computed without accounting for the vacuum polarization effects (QED-OFF). With the selected t_{exp}, the QED-OFF model is always rejected with high confidence, with typical values of reduced $\chi^2 \gtrsim 4$ versus 1.13–1.58. We note that the present treatment of the QED-OFF case differs slightly from that described in Taverna et al. (2014) inasmuch the adiabatic radius is artificially moved to the last-scattering radius/star surface for photons which do/do not undergo scatterings. To all effects this results in an overestimate of the polarization degree calculated in the QED-OFF case. With reference to Fig. 13, a polarization measure $\gtrsim 20$ per cent will be sufficient to validate vacuum birefringence effects in strong magnetic fields.

Because of the comparatively low polarization degree expected in the condensed surface models, the errors on both the polarization fraction and angle are much larger than in the blackbody and the atmosphere cases. In order to verify if results are strongly dependent on the exposure time, we produced a further (fixed-ion) simulation with $t_{exp} = 2$ Ms (see Fig. 14). While the error bars are sensibly reduced and the robustness of the QED-ON versus QED-OFF fits improves, the model parameters turn out to be fully compatible with those of the 1 Ms simulation (see Table 2). Fig. 15 shows the same simulations as in Fig. 13, but assuming the 2–10 keV unabsorbed flux of the AXP 4U 0142+61 (i.e. ~3 times higher than that used previously). As expected, results in this case (see Table 3) are fully compatible with those obtained previously; in particular, the higher value of the flux allows us to reduce the exposure time (by a factor of ~2) and still get the same level of accuracy.

---

[11]Results for free-ions are very similar and are not shown.

Given the vastly different expectations for the polarization degree and angles from the different models discussed above, phase-resolved polarimetry may provide a direct way to probe the physical state of a magnetar surface. To test this, we produced synthetic data from the atmosphere model and fit them both with the atmosphere archive and the condensed surface one (free-ions). Results are reported in Fig. 16. While the input model parameters are well recovered by the fit ($\chi^2_{red} = 1.17$) in the former case, the agreement between the data and the best condensed surface model is largely unacceptable ($\chi^2_{red} = 160.6$, see Table 4). This result is robust and shows that there is no degeneracy in the model fit at variance with what occurs considering phase averaged polarization observables (see Taverna et al. 2015; González Caniulef et al. 2016).

6 DISCUSSION AND CONCLUSIONS

In this work the spectral and polarimetric properties of persistent X-ray emission from magnetar sources have been investigated within the RCS paradigm, first suggested by Thompson et al. (2002). The present study improves over previous ones (Fernández & Thompson 2007; Nobili et al. 2008; Fernández & Davis 2011; Taverna et al. 2014) inasmuch more physical surface emission models have been considered: a magnetized hydrogen atmosphere and a condensed surface. The feasibility of polarization measurements in magnetars with the forthcoming X-ray polarimeter *IXPE* was also readdressed. Our main findings are as follows:

(i) while the spectral properties are not very sensitive to the surface emission model (showing always a 'blackbody+power-law' shape), the polarization pattern is strongly affected by the primary photon spectrum;

(ii) atmospheric models exhibit a high polarization degree in the X-mode (up to ~ 80 per cent), depending on the geometrical and magnetospheric parameters, not much below that of 100 per cent polarized blackbody seed photons;

(iii) condensed surface models (both in the free- and fixed-ion limits) are much less polarized (up to ~ 30 per cent) and O-mode photons dominate in the low-energy range;

(iv) RCS acts in depolarizing the (highly polarized) atmospheric seed photons as they propagate in the magnetosphere, while the opposite occurs for the (weakly polarized) condensed surface ones; as a consequence, at large energies, the polarization degree approaches in any case 33 per cent (the value expected from the RCS cross-sections) but it does so either from above or from below, respectively;

(v) simulations of *IXPE* response show that an exposure time of 0.5–1 Ms is sufficient to measure the polarization observables in a bright magnetar source, with high enough accuracy to probe (i) vacuum birefringence and (ii) the physical state of the NS surface.

Previous results were obtained under a number of assumptions, concerning the description of both the star magnetosphere and the surface temperature distribution. In addition, no GR effects (see e.g. Fernández & Davis 2011; Taverna et al. 2015) have been accounted for.

Crustal displacements in a magnetar most likely produce a localized twist, confined to a bundle of current-carrying field lines. Moreover, the twist itself decays, shrinking towards the polar regions. As a consequence, the star surface should exhibit hotspot(s) in correspondence to the footpoints of the twisted field lines, where returning currents dissipate, while the rest of the surface is at a lower temperature. The size of the hotspot(s) decreases as the magnetosphere untwists (Beloborodov 2009). Actually, our Monte
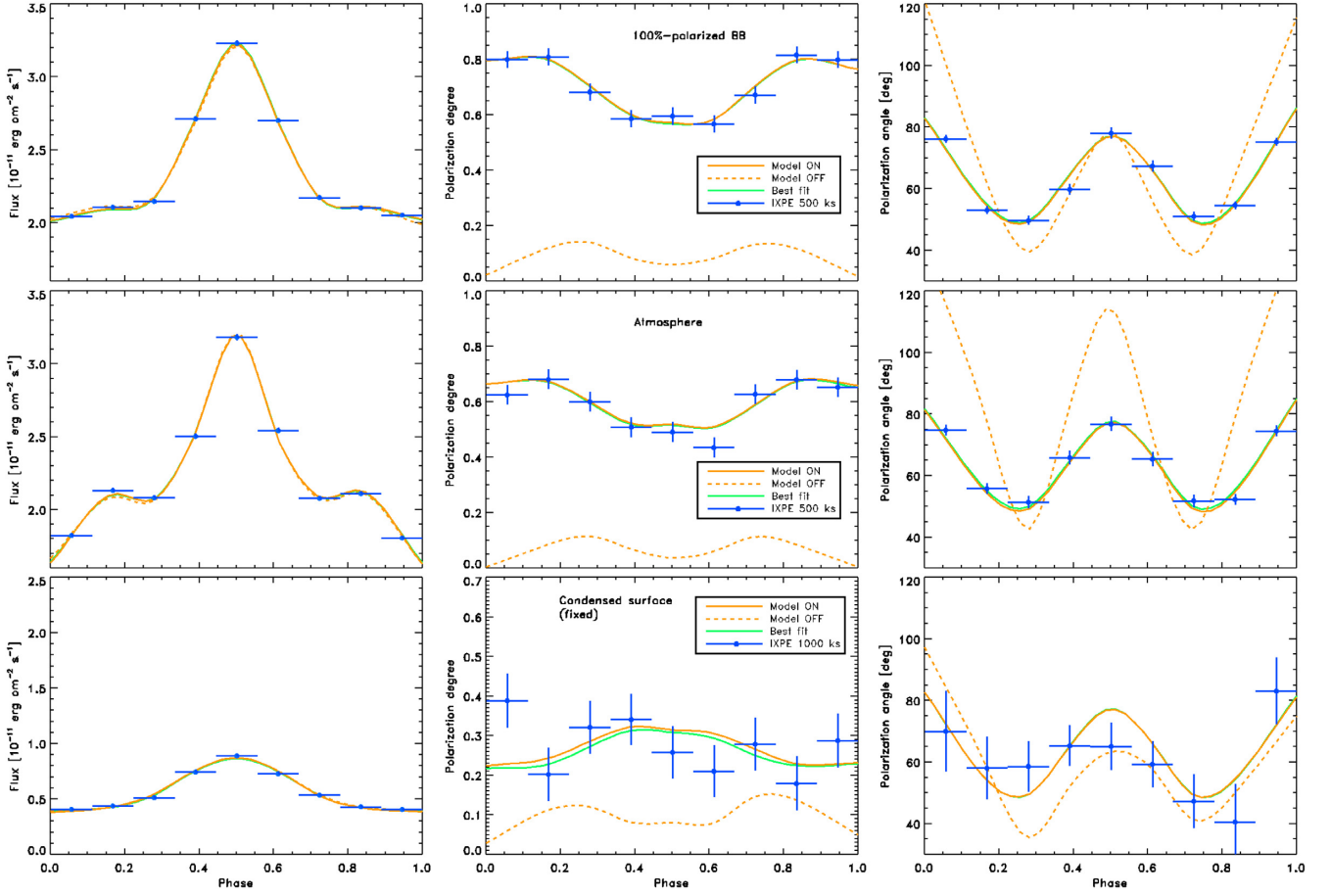
Figure 13. Flux (left column), linear polarization degree (middle column), and polarization angle (right column) as functions of the rotational phase for blackbody (100 per cent polarized seed photons, top row), atmosphere (middle row), and condensed surface (fixed-ion limit, bottom row). The model parameters are $B_{\rm p} = 5 \times 10^{14}$ G, $\Delta\phi_{\rm N-S} = 0.5$ rad, $\beta = 0.34$, $\chi = 90°$, and $\xi = 60°$. The surface temperature and the 2–10 keV unabsorbed flux are 0.5 keV and 2.4×10^{-11} erg cm^{-2} s^{-1}, respectively, as appropriate for J1708. Filled circles with error bars (at 1σ) are the simulated data. The orange and green solid lines show the model from which data were obtained and the best simultaneous fit, respectively. The orange dashed lines refer to the QED-OFF case (see text for more details).

Table 2. Results of the simultaneous fits of the flux, linear polarization degree, and polarization angle shown in Figs 13 and 14, in the case of 100 per cent polarized blackbody, atmosphere, and condensed surface (fixed-ions) models, either with QED effects (QED-ON) or without (QED-OFF). The reduced χ^2 for the OFF models is the minimum among the different realizations. Reported errors are at the 1σ level.

	$t_{\rm exp}$ (ks)	χ (deg)	ξ (deg)	$\Delta\phi_{\rm N-S}$ (rad)	β	$\chi^2_{\rm red}$
Input values	–	90	60	0.5	0.34	–
100 per cent polarized BB						
QED-ON	500	90.80 ± 1.27	59.53 ± 0.90	0.502 ± 0.019	0.340 ± 0.008	1.14
QED-OFF	500	102.51 ± 1.17	49.80 ± 0.79	0.300 ± 0.000[a]	0.411 ± 0.005	137.1
Atmosphere						
QED-ON	500	90.35 ± 1.01	59.28 ± 1.01	0.507 ± 0.025	0.334 ± 0.013	1.58
QED-OFF	500	91.31 ± 0.71	56.30 ± 0.73	0.348 ± 0.011	0.445 ± 0.007	103.2
Condensed surface (fixed-ions)						
QED-ON	1000	88.81 ± 7.27	60.85 ± 4.31	0.522 ± 0.053	0.324 ± 0.026	1.13
QED-OFF	1000	93.74 ± 6.71	65.96 ± 2.70	0.450 ± 0.021	0.355 ± 0.011	2.38
Condensed surface (fixed-ions)						
QED-ON	2000	91.89 ± 4.64	59.57 ± 2.44	0.511 ± 0.030	0.337 ± 0.017	1.16
QED-OFF	2000	98.20 ± 3.44	53.65 ± 1.79	0.468 ± 0.017	0.354 ± 0.011	3.95

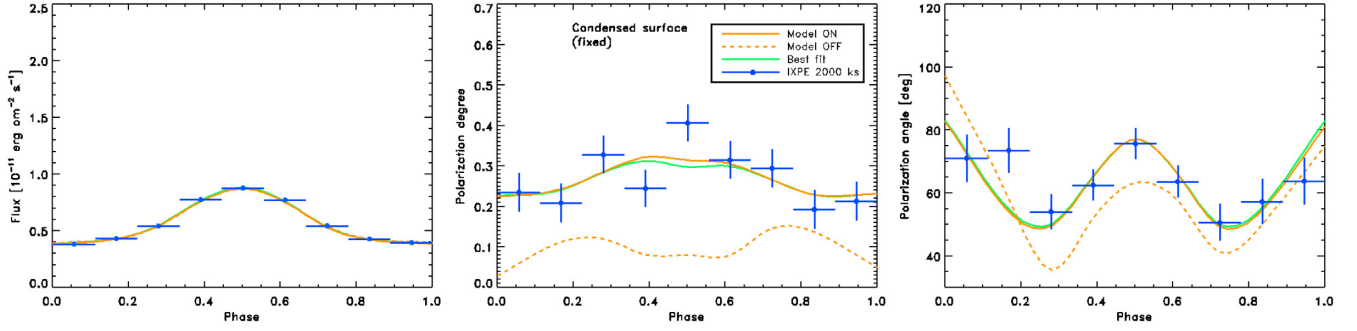[a]During the fit this parameter hit the lower bound of the range.

Figure 14. Same as in Fig. 13 (bottom row), but for $t_{exp} = 2$ Ms.
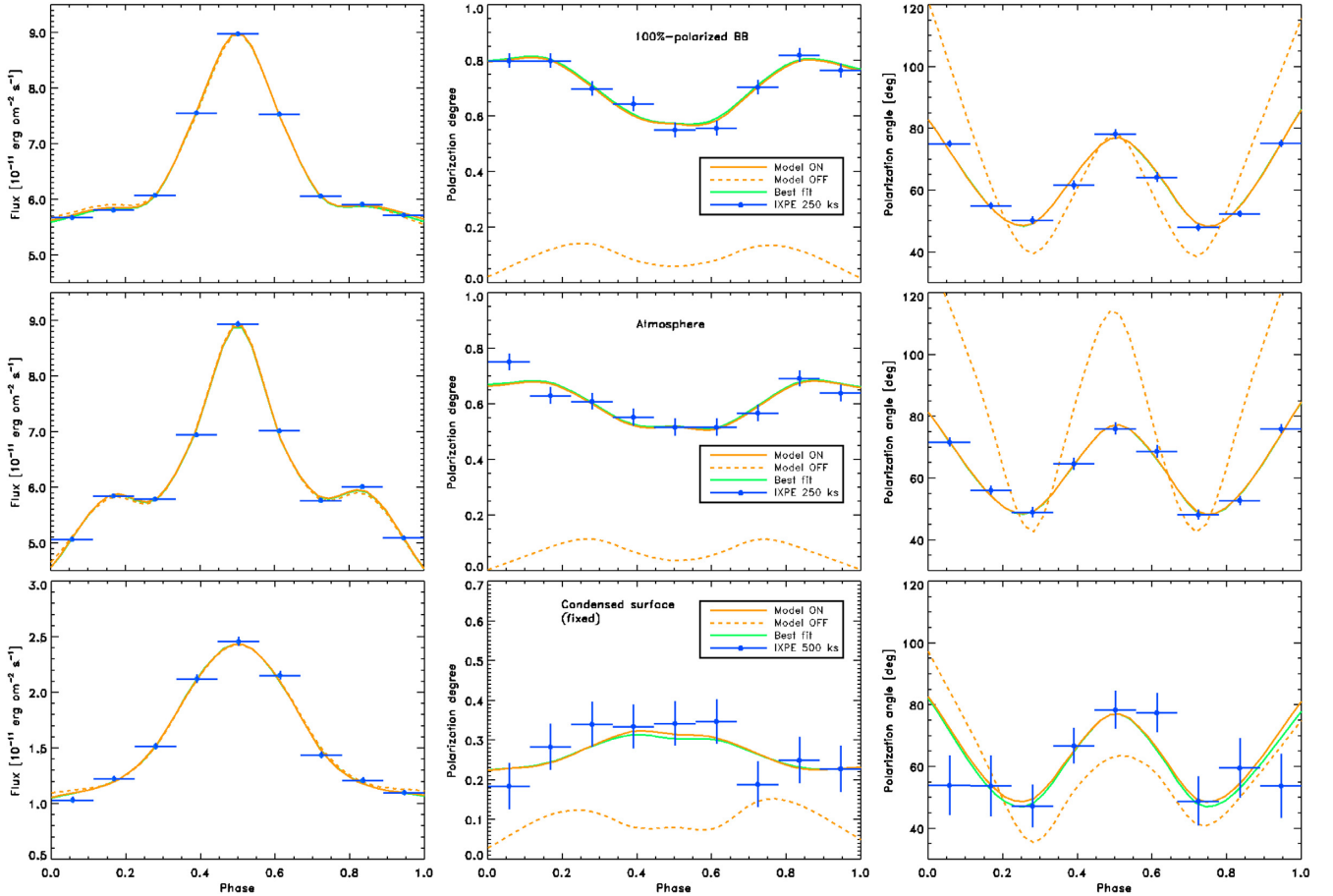

Figure 15. Same as in Fig. 13 but with 2–10 keV unabsorbed flux of 6.9×10^{-11} erg cm^{-2} s^{-1} as for AXP 4U 0142+61. An exposure time of 250 ks has been considered for blackbody and atmosphere mock data, while $t_{exp} = 500$ ks is taken for the condensed surface case.

carlo code can handle quite general magnetic field configurations, so that in principle it would have been possible to treat a localized twist (see e.g. Viganò et al. 2012). Also the surface temperature can be specified without restrictions, assigning a different value to each patch (see Nobili et al. 2008).

In this work, however, we used a simpler description in which the magnetosphere is globally twisted (i.e. the entire north magnetic hemisphere is twisted wrt the south one), the current flow is unidirectional (i.e. charge carriers are electrons), and the temperature is constant over the entire surface. The reason for this choice is two-fold: first, it allows for a direct comparison with previous works (Fernández & Thompson 2007; Nobili et al. 2008;

Fernández & Davis 2011; Taverna et al. 2014), as already mentioned in Section 2.1, and secondly, it avoids to introduce a large number of free parameters, which would have been necessary to describe a more complex magnetospheric structure and temperature profile.

The charge carriers flowing along the closed field lines are expected to be mostly electrons and positrons (Beloborodov & Thompson 2007), with a (spatially) changing Lorentz factor, as discussed in some more detail by Beloborodov (2013). In the lack of a complete model, which is still to come, we retained both the unidirectional flow hypothesis and the assumptions that charges move with a constant speed.

Table 3. Same as in Table 2 but for the case shown in Fig. 15.

	t_{exp} (ks)	χ (deg)	ξ (deg)	$\Delta\phi_{N-S}$ (rad)	β	χ^2_{red}
Input values	–	90	60	0.5	0.34	–
100 per cent polarized BB						
QED-ON	250	90.61 ± 1.13	59.73 ± 0.78	0.489 ± 0.016	0.349 ± 0.007	1.16
QED-OFF	250	103.68 ± 0.97	48.48 ± 0.65	0.300 ± 0.000^a	0.412 ± 0.004	191.3
Atmosphere						
QED-ON	250	90.01 ± 0.87	59.92 ± 0.86	0.491 ± 0.022	0.347 ± 0.011	1.53
QED-OFF	250	91.82 ± 0.59	55.38 ± 0.62	0.350 ± 0.009	0.450 ± 0.006	140.2
Condensed surface (fixed-ions)						
QED-ON	500	87.85 ± 6.74	62.06 ± 3.53	0.502 ± 0.031	0.341 ± 0.017	1.14
QED-OFF	500	99.85 ± 4.33	54.49 ± 1.95	0.433 ± 0.025	0.376 ± 0.015	3.01
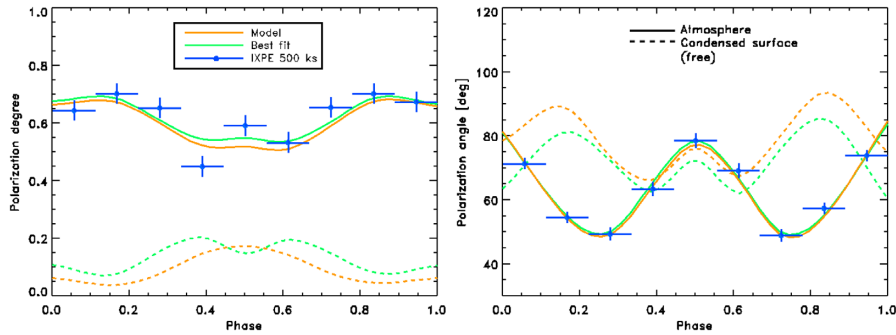
Figure 16. Linear polarization degree (left) and angle (right) as functions of the rotational phase for $B_p = 5 \times 10^{14}$ G, $\Delta\phi_{N-S} = 0.5$ rad, $\beta = 0.34$, $\chi = 90°$, $\xi = 60°$, and the 2–10 keV unabsorbed flux of J1708 ($t_{exp} = 500$ ks). Filled circles with error bars (at 1σ) are the simulated data obtained from the atmosphere model in the 2–8 keV band (orange solid line); the condensed surface (free-ion) model for the same values of the parameters is shown by the orange dashed curve. The green lines represent the best simultaneous fits for the atmosphere (solid) and the condensed surface (dashed) models.

Table 4. Results of the simultaneous fits of the linear polarization degree and polarization angle shown in Fig. 16. The reduced χ^2 for the condensed surface model is the minimum among the different realizations. Reported errors are at the 1σ level.

	χ (deg)	ξ (deg)	$\Delta\phi_{N-S}$ (rad)	β	χ^2_{red}
Input values	90	60	0.5	0.34	–
Fitting models					
Atmosphere	87.54 ± 2.92	58.25 ± 1.93	0.470 ± 0.061	0.342 ± 0.081	1.19
Condensed surface (free-ions)	92.34 ± 1.38	75.44 ± 1.41	0.920 ± 0.052	0.200 ± 0.000^a	165.1

The surface temperature distribution in a magnetar is governed by a number of different and competing effects, which are still not completely understood. Under magnetar conditions electron transport in the envelope, which can be assumed to be the main responsible for heat conduction, occurs almost entirely along the magnetic field lines. This produces a substantial temperature variation in going from the magnetic poles to the equator (see e.g. Potekhin, Pons & Page 2015), which can potentially modify both the spectral and polarization properties of magnetar persistent radiation. On the other hand, heating by returning currents can dominate over the internal one, making the equatorial belt hotter (Beloborodov & Thompson 2007). In the light of this, an isothermal surface distribution may be not too far from the realistic one, and will in any case catch the essential features of the model. We stress again that the effects of returning currents on the surface star layers are ignored.

In the case of thermally emitting NSs, vacuum birefringence strongly influences the polarization properties at infinity. QED effects are actually quite sensitive to the extent of the radiating region on the star surface or, equivalently, on the steepness of the temperature gradient. As discussed in van Adelsberg & Perna (2009), if emission in these sources comes from a small (point-like) polar cap, the depolarization due to geometrical effects is not present, so that expectations from QED-ON and QED-OFF models are quite the same. In order to test vacuum birefringence through the measured polarization degree, the cap aperture should be $\gtrsim 40°$ (González Caniulef et al. 2017; Santangelo et al. 2019b). Clearly, in magnetars RCS acts in spatially redistributing surface photons. If indeed primary photons come from a small cap, we expect the QED-ON and QED-OFF models to produce nearly the same results only (or mostly) below ∼2 keV, where unscattered radiation dominates.

Predictions for the polarization observables in the atmospheric case are quite dependent on the adopted treatment of the mode switching at the vacuum resonance, since this strongly influences the opacities. As a matter of fact, at the mode collapse points (vacuum resonances) the normal modes approximation breaks down

and radiative transfer should be solved using the Stokes parameters (see Pavlov & Shibanov 1979; Lai & Ho 2003). The two limiting cases of full mode conversion and no mode conversion have been investigated (Ho & Lai 2003) and both lead to a large polarization of radiation emerging from a single patch ($\sim$ 100 per cent in the soft X-ray band). In this work we assumed adiabatic mode conversion at the resonance and treated the mode switching following van Adelsberg & Lai (2006). Although their approach is formally energy and angle dependent, under the conditions typical of the atmospheres presented here, most photons actually undergo mode switching at the resonance. On the other hand, the critical angle at which the normal modes break down is strongly dependent on photon frequency and direction (Pavlov & Shibanov 1979), so that the differences in the X- and O-mode opacities induced by the strong field are much reduced when partial mode switching occurs. This may lead to a much smaller degree of polarization (see also González Caniulef et al. 2019, for a detailed discussion in the grey case).

ACKNOWLEDGEMENTS

REFERENCES

Albano A., Turolla R., Israel G. L., Zane S., Nobili L., Stella L., 2010, ApJ, 722, 788
Baumgartner W. H., Strohmayer T., Kallman T., Black J. K., Hill J. E., Swank J. H., Jahoda K. M., 2012, Proc. SPIE Conf. Ser. Vol. 8443, Space Telescopes and Instrumentation 2012: Ultraviolet to Gamma Ray. SPIE, Bellingham, p. 84434K
Bellazzini R., Costa E., Matt G., Tagliaferri G., 2010, X-ray Polarimetry: A New Window in Astrophysics. Cambridge Univ. Press, Cambridge
Beloborodov A. M., 2002, ApJ, 566, L85
Beloborodov A. M., 2009, ApJ, 703, 1044
Beloborodov A. M., 2013, ApJ, 777, 114
Beloborodov A. M., Thompson C., 2007, ApJ, 657, 967
Brinkmann W., 1980, A&A, 82, 352
Connors P. A., Stark R. F., 1977, Nature, 269, 128
Connors P. A., Piran T., Stark R. F., 1980, ApJ, 235, 224
Costa E., Soffitta P., Bellazzini R., Brez A., Lumb N., Spandre G., 2001, Nature, 411, 662
Dib R., Kaspi V. M., 2014, ApJ, 784, 37
Duncan R. C., Thompson C., 1992, ApJ, 392, L9
Feng H. et al., 2019, Exp. Astron., 47, 225
Fernández R., Davis S. W., 2011, ApJ, 730, 131
Fernández R., Thompson C., 2007, ApJ, 660, 615
Ginzburg V. L., 1970, The Propagation of Electromagnetic Waves in Plasmas, 2nd rev. and enl. ed. Pergamon, Oxford
Gnedin Yu. N., Pavlov G. G., 1973, Zh. Eksper. Teor. Fiz., 65, 1806(English transl.: 1974, Sov. Phys.–JETP, 38, 903)
González Caniulef D., Zane S., Taverna R., Turolla R., Wu K., 2016, MNRAS, 459, 3585
González Caniulef D., Zane S., Taverna R., Turolla R., Song X., Wu K., 2017, J. Phys. Conf. Ser., 932, 012024
González Caniulef D., Zane S., Turolla R., Wu K., 2019, MNRAS, 483, 599
Güver T., Göğüş E., Özel F., 2015, ApJ, 801, 48
Harding A. K., Lai D., 2006, Rep. Prog. Phys., 69, 2631

Heyl J. S., Shaviv N. J., 2000, MNRAS, 311, 555
Heyl J. S., Shaviv N. J., 2002, Phys. Rev. D., 66, 023002
Ho W. C. G., Lai D., 2003, MNRAS, 338, 233
Ho W. C. G., Potekhin A. Y., Chabrier G., 2008, ApJSS, 178, 102
Jahoda K. et al., 2014, Proc. SPIE Conf. Ser. Vol. 9144, Space Telescopes an Instrumentation 2014: Ultraviolet to Gamma Ray. SPIE, Bellingham, p. 91440N
Kaspi V. M., Beloborodov A. M., 2017, ARA&A, 55, 261
Kiss M., Pearce M., 2007, NIMPA, 580, 876
Lai D., 2001, Rev. Mod. Phys., 73, 629
Lai D., Ho W. C. G., 2002, ApJ, 566, 373
Lai D., Ho W. C. G., 2003, ApJ, 588, 962
Lai D., Salpeter E. E., 1997, ApJ, 491, 270
Larsson S., Pearce M., 2004, Nucl. Instrum. Methods Phys. Res. A, 525, 148
Medin Z., Lai D., 2006, Phys. Rev. A, 74, 062508
Medin Z., Lai D., 2007, MNRAS, 382, 1833
Mészáros P., 1992, High-Energy Radiation from Magnetized Neutron Stars. Univ. Chicago Press, Chicago
Nobili L., Turolla R., Zane S., 2008, MNRAS, 386, 1527
Olausen S. A., Kaspi V. M., 2014, ApJS, 212, 6O
Pavan L., Turolla R., Zane S., Nobili L., 2009, MNRAS, 395, 753
Pavlov G. G., Shibanov Y. A., 1978, SvA, 22, 214
Pavlov G. G., Shibanov Y. A., 1979, Sov. J. Exp. Theor. Phys., 49, 741
Pavlov G. G., Shibanov Y. A., Ventura J., Zavlin V. E., 1994, A&A, 289, 837
Pérez-Azorín J. F., Miralles J. A., Pons J. A., 2005, A&A, 433, 275
Potekhin A. Y., 2014, Phys. Usp., 57, 735
Potekhin A. Y., Lai D., Chabrier G., Ho W. C. G., 2004, ApJ, 612, 1034
Potekhin A. Y., Suleimanov V., van Adelsberg M., Werner K., 2012, A&A, 546, A121
Potekhin A. Y., Chabrier G., Ho W. C. G., 2014, A&A, 572, A69
Potekhin A. Y., Pons J. A., Page D., 2015, Space Sci. Rev., 191, 239
Press W. H., Teukolsky S. A., Vetterling W. T., Flannery B. P., 1992, Numerical Recipies. Cambridge Univ. Press, Cambridge
Rea N., Esposito P., 2011, in Torres D. F., Rea N., eds, Astrophysics and Space Science Proceedings, High-Energy Emission from Pulsars and Their Systems. Springer-Verlag, Berlin, p. 247
Rea N. et al., 2007a, Ap&SS, 308, 505
Rea N. et al., 2007b, MNRAS, 381, 293
Rea N. et al., 2010, Science, 330, 944
Romani R. W., 1987, ApJ, 313, 718
Santangelo A. et al., 2019a, Sci. China Phys. Mech. Astron., 62, 29502
Santangelo A. et al., 2019b, Sci. China Phys. Mech. Astron., 62, 29505
Shibanov I. A., Zavlin V. E., Pavlov G. G., Ventura J., 1992, A&A, 266, 313
Soffitta P., Costa E., Bozzo E. et al., 2016, Proc. SPIE Conf. Ser. Vol. 9905, Space Telescopes and Instrumentation 2016: Ultraviolet to Gamma Ray, 990515. SPIE, Bellingham, p. 990515
Stark R. F., Connors P. A., 1977, Nature, 266, 429
Suleimanov V., Potekhin A. Y., Werner K., 2009, A&A, 500, 891
Taverna R., Turolla R., 2017, MNRAS, 469, 3610
Taverna R., Muleri F., Turolla R., Soffitta P., Fabiani S., Nobili L., 2014, MNRAS, 438, 1686
Taverna R., Turolla R., González Caniulef D., Zane S., Muleri F., Soffitta P., 2015, MNRAS, 454, 3254
Thompson C., Duncan R. C., 1995, MNRAS, 275, 255
Thompson C., Lyutikov M., Kulkarni S. R., 2002, ApJ, 574, 332
Turolla R., 2009, in Becker W., ed., Astrophysics and Space Science Library, Vol. 357, Neutron Stars, and Pulsars. Springer-Verlag, Berlin, p. 141
Turolla R., Nobili L., 2013, ApJ, 768, 147
Turolla R., Zane S., Drake J. J., 2004, ApJ, 603, 265
Turolla R., Zane S., Watts A. L., 2015, Rep. Prog. Phys., 78, 11
van Adelsberg M., Lai D., 2006, MNRAS, 373, 1495
van Adelsberg M., Perna R., 2009, MNRAS, 399, 1523
van Adelsberg M., Lai D., Potekhin A. Y., Arras P., 2005, ApJ, 628, 902
Viganò D., Parkins N., Zane S., Turolla R., Pons J. A., Miralles J. A., 2012, JPhCS, 342, 012013

von Neumann J., 1951, Nat. Bureau Standards, 12, 36

Weisskopf M. C., Silver E. H., Kastenbaum K. S., Long K. S., Novick R., Wolff R. S., 1978, ApJ, 220, L117

Weisskopf M. C. et al., 2016, Proc. SPIE Conf. Ser. Vol. 9905, Space Telescopes and Instrumentation, Ultraviolet to Gamma Ray. SPIE, Bellingham, p. 990517

Weisskopf M. C., 2018, Galaxies, 6, 33

Zane S., Turolla R., 2006, MNRAS, 366, 727

Zane S., Rea N., Turolla R., Nobili L., 2009, MNRAS, 398, 1403

Zhang S. et al., 2019, Sci. China Phys. Mech. Astron., 62, 29502

This paper has been typeset from a TEX/LATEX file prepared by the author.